

Time-dependent density-functional theory for periodic solids: assessment of excitonic exchange-correlation kernels

Young-Moo Byun

Department of Physics, University of Illinois at Chicago, Chicago, IL 60607, USA

Jiuyu Sun

Department of Physics and Astronomy, University of Missouri, Columbia, MO 65211, USA

Carsten A. Ullrich

Department of Physics and Astronomy, University of Missouri, Columbia, MO 65211, USA

Abstract. We review recent theoretical and computational developments in time-dependent density-functional theory (TDDFT) for periodic insulators and semiconductors. To capture excitonic effects within a linear-response TDDFT framework requires using exchange-correlation (xc) kernels with a proper long-range behavior, which can be efficiently modeled with a class of so-called long-range corrected xc kernels. While attractive from a computational standpoint, these xc kernels have their limitations and require judicious use. We review the pros and cons of various xc kernels in the literature, and discuss an empirical scaling approach to obtain accurate exciton binding energies with TDDFT. We also discuss generalized TDDFT approaches for excitons using hybrid functionals.

1. Introduction

Among the most important properties of a material is the way in which it responds to incident light. The optical response of a material is determined by the macroscopic dielectric function $\epsilon_{\text{mac}}(\omega)$, which depends on the light frequency ω [1]. The calculation of $\epsilon_{\text{mac}}(\omega)$ from first principles, which allows a direct comparison with experimental optical spectra, is one of the prime tasks of electronic structure theory. Depending on the material at hand, this can be quite a formidable challenge, especially if subtle spectral features such as excitons are to be accurately described.

A quantum mechanical description of the electronic structure and excitations in matter can be accomplished in more than one way. One approach, often referred to as many-body perturbation theory, is based on the concept of *quasiparticles*: the addition and removal of quasiparticles is described via Green's functions, and excitation processes involving quasidelectron- and -hole pairs, including their screened interaction, are treated using suitably defined correlation functions [2–5]. An alternative approach is based on the electronic *density*: the electronic ground state is obtained using density-functional theory (DFT) [6–8], and the dynamics is described with time-dependent density-functional theory (TDDFT) [9–11], where all the physics of electronic excitations is implicitly encoded in the fluctuations of the time-dependent density. Both approaches are formally exact, and require approximations to be used in practice; both approaches have their own advantages and drawbacks.

It is often said that the “gold standard” for calculating electronic excitations in materials is via many-body perturbation theory, using the Bethe-Salpeter equation (BSE) [12–18], usually combined with the *GW* approximation for the electronic quasiparticle band structure [19, 20]. The *GW*/BSE approach is nowadays routinely applied to a broad variety of systems and materials [21–29], and is available in several noncommercial software platforms [30–34]. However, the *GW*/BSE approach, which is based on many-body Green's functions, tends to be computationally expensive, which precludes its applications to systems beyond a certain degree of complexity.

As discussed above, an alternative to many-body perturbation theory is TDDFT [9–11]. TDDFT is formally exact and therefore yields, in principle, the exact excitation energies and optical spectra of any type of material: atoms, molecules, and periodic or nonperiodic extended systems. In contrast with many-body theories based on Green's functions, which are functions of two or more spatial variables, TDDFT is based on the particle density, which depends on a single spatial variable only; this promises to make TDDFT computationally more efficient. However, the catch is that a crucial ingredient, namely the exchange-correlation (xc) potential, needs to be approximated, and the computational efficiency of TDDFT and the quality of results critically depend on the choice of approximation.

In this review article, we will focus on a particular class of approximations to the so-called xc kernel of linear-response TDDFT, known as long-range corrected (LRC) approximations. The frequency-dependent xc kernel of TDDFT is formally defined

within the linear-response framework as [35]

$$f_{\text{xc}}(\mathbf{r}, \mathbf{r}', \omega) = \int d(t-t') e^{i\omega(t-t')} \left. \frac{\delta v_{\text{xc}}[n](\mathbf{r}, t)}{\delta n(\mathbf{r}', t')} \right|_{n_0(\mathbf{r})}, \quad (1)$$

where $v_{\text{xc}}[n](\mathbf{r}, t)$ is the xc potential of TDDFT [a functional of the time-dependent density $n(\mathbf{r}, t)$], and $n_0(\mathbf{r})$ is the ground-state density of the unperturbed system. For spatially periodic solids (the only type of system we will consider here), the xc kernel is transformed into reciprocal space, $f_{\mathbf{G}\mathbf{G}'}^{\text{xc}}(\mathbf{q}, \omega)$, where \mathbf{q} is a wave vector within the first Brillouin zone (BZ) and \mathbf{G} and \mathbf{G}' are reciprocal lattice vectors.

Linear-response TDDFT provides a formally exact framework for calculating electronic excitations [36, 37]. In particular, $\epsilon_{\text{mac}}(\omega)$ can be rigorously obtained from TDDFT. In Section 3 we will review the TDDFT linear-response framework for the optical response of periodic solids with a gap, i.e., insulators and semiconductors (for earlier reviews on this subject see [2, 38–41]).

Of course, no TDDFT calculation is exact except for the very simplest of model systems, since all practical calculations necessarily involve three distinct approximations: (1) the electronic ground state (i.e., the Kohn-Sham band structure) must be obtained with an approximate xc potential $v_{\text{xc}}^{\text{app}}(\mathbf{r})$; (2) the linear-response TDDFT calculation must be carried out with an approximate xc kernel $f_{\text{xc}}^{\text{app}}(\mathbf{r}, \mathbf{r}', \omega)$; (3) all computations require some form of numerical discretization, either in the form of a finite basis or of a real-space grid with finite spacing; in addition, many codes work with pseudopotentials, which reduces the computational burden but introduces further approximations.

While all of this is well known, up until not too long ago it was quite commonly believed that “TDDFT cannot do excitons”. The reason being that the standard xc functionals that had been so successful in condensed matter, the local-density approximation (LDA) and generalized-gradient approximations (GGAs) and their adiabatic counterparts for the time-dependent case (ALDA and AGGA), indeed perform very poorly when it comes to describing excitonic features in insulators and semiconductors.

The reason for the failure of ALDA and AGGAs to capture excitons is now well understood. The existence of excitons requires a screened electron-hole interaction which, in the TDDFT picture, is entirely due to the xc kernel. More precisely, it is due to a key feature of the exact xc kernel, namely the fact that it has a long spatial range in systems with a gap: in real space, $f_{\text{xc}} \sim -|\mathbf{r} - \mathbf{r}'|^{-1}$ in the limit of large separation, and in reciprocal space $f_{\text{xc}} \sim -1/q^2$ in the limit of small wave vector. Semilocal functionals such as ALDA and AGGA, on the other hand, are spatially short-ranged, and their electron-hole interaction is orders of magnitude too weak in extended solids (they still work fine in small finite systems such as atoms and molecules).

In a series of groundbreaking papers beginning 2002 [2, 42–51], the connection between the long-range behavior of f_{xc} and excitons was revealed and analyzed, and important proof of concept was given that TDDFT is indeed capable of producing excitonic effects with similar accuracy as the BSE, provided the right physics is built

into the approximate xc kernel. This can be accomplished using a reverse-engineering approach [42], using input from many-body theory and constructing an xc kernel which can be viewed as an effective localized BSE; unsurprisingly, this is computationally quite costly.

Approximate xc kernels of a much simple form which are designed to have the right long-range behavior became known as “long-range corrected” (LRC) kernels [49]. Today, there exists a whole family of LRC kernels in TDDFT, and in Sections 4 and 5 of this article we will review them and critically assess their performance. It turns out that there are pros and cons: LRC kernels are numerically cheap and successfully capture exciton binding, but they tend to work for parts of the spectrum only. We will conclude this review with alternative TDDFT-based approaches, based on the idea of hybrid functionals, which may hold considerable promise for future applications.

2. The Wannier model

We begin with a discussion of the time-honored Wannier-Mott model of excitons [52,53], because this provides us with some insights which will be useful later on. According to this model, excitons are described as effective two-particle systems, where an electron is bound to a hole via screened Coulomb interaction (see insert of Fig. 1a). The model can be derived from many-body theory [5,12] by using a two-band approximation whereby the electronic band structure is reduced to one occupied valence band and one empty conduction band, both taken to be parabolic. This then allows one to invoke the effective-mass approximation [54, 55], where conduction band electrons have effective mass m_e^* and valence band holes have effective mass m_h^* , and the exciton reduced effective mass is $m_r = m_e^* m_h^* / (m_e^* + m_h^*)$. Excitons are then described by the following hydrogen-like Schrödinger equation [56]:

$$\left\{ -\frac{\hbar^2 \nabla^2}{2m_r} - \frac{e^2}{4\pi\epsilon_0\epsilon r} \right\} \psi_n(\mathbf{r}) = E_n \psi_n(\mathbf{r}). \quad (2)$$

Here, ϵ_0 is the vacuum permittivity, e is the free electron charge, and ϵ is the dielectric constant of the material.

Equation (2), which is also known as the Wannier equation, yields a Rydberg series of bound states as well as a continuum of unbound states. The 3D exciton bound-state energies are given by

$$E_n = -E_0 \frac{1}{n^2}, \quad n = 1, 2, \dots, \quad (3)$$

where E_0 , the binding energy of the lowest exciton, is

$$E_0 = \frac{\hbar^2}{2m_r a_0^2}, \quad (4)$$

and the exciton Bohr radius a_0 is

$$a_0 = \frac{\hbar^2 \epsilon_0}{e^2 m_r}. \quad (5)$$

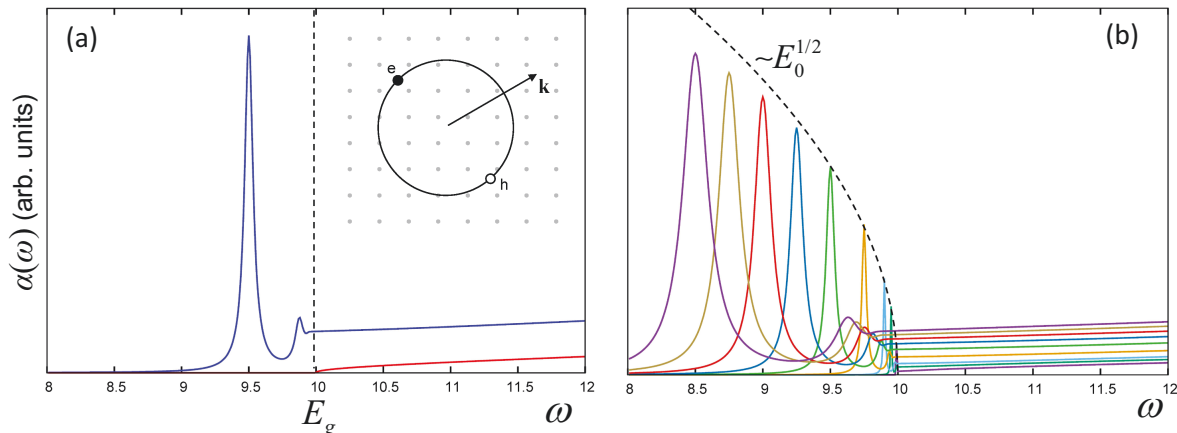


Figure 1. Absorption spectrum of the Wannier model, see Eq. (6). (a) Comparison of excitonic spectrum (blue) with independent-particle spectrum (red). The dashed vertical line shows the position of the band gap. The insert shows the exciton as a bound electron-hole pair with center-of-mass momentum \mathbf{k} . (b) Absorption spectra with different exciton binding energies, illustrating the fact that the oscillator strength of the excitonic peaks near the band edge grows as $E_0^{1/2}$.

As an example, consider the lowest bound exciton in GaAs, a material in which the Wannier equation works particularly well: one obtains $E_0 = 4.6$ meV and $a_0 = 118$ Å (for comparison, the experiment gives $E_0^{\text{exp}} = 4.2$ meV). This clearly shows that Wannier excitons are weakly bound and extend over many lattice constants, thus justifying the effective-mass treatment of Eq. (2).

Using the hydrogenic wave functions of the Wannier model, it is possible to derive a closed expression for the optical absorption spectrum in the neighborhood of the band edge [56]:

$$\alpha(\omega) = \frac{2|d_{cv}|^2 \hbar\omega}{\hbar n_b c a_0^3 E_0} \left[\sum_{n=1}^{\infty} \frac{4\pi}{n^3} \delta\left(\Delta + \frac{1}{n^2}\right) + \theta(\Delta) \frac{\pi e^{\pi/\sqrt{\Delta}}}{\sinh(\pi/\sqrt{\Delta})} \right], \quad (6)$$

where $\Delta = (\hbar\omega - E_g)/E_0$ describes the detuning from the band gap E_g , d_{cv} is the optical dipole matrix element between valence and conduction band, and n_b is the background refractive index. Equation (6) is also known as the Elliott formula [55].

Figure 1a illustrates the absorption spectrum resulting from an evaluation of the Elliott formula (6) using dimensionless units (blue line). The input parameters are $E_g = 10$, $E_0 = 0.5$, and an artificial line broadening of 0.05. A very pronounced first excitonic peak at $\omega = 9.5$ is observed; the exciton Rydberg series merges smoothly with the continuum. For comparison, the independent-particle spectrum (red line) has a much lower oscillator strength near the band edge.

We now want to know how the oscillator strength of the lowest exciton scales with its binding energy. We evaluate the Elliott formula for $\omega = E_g - E_0$, so that $\Delta = 1$, and

$$\alpha(E_g - E_0) = \frac{8\pi|d_{cv}|^2 (E_g - E_0)}{n_b c a_0^3 E_0}. \quad (7)$$

But we can express a_0 in terms of E_0 via Eq. (4), so that

$$\alpha(E_g - E_0) = \frac{8\pi|d_{cv}|^2(2m_r)^{3/2}}{n_b c \hbar^3} (E_g - E_0) \sqrt{E_0}. \quad (8)$$

Let us assume that $E_g \gg E_0$, which is clearly the case in situations where the Wannier model is valid. We then find that

$$\alpha \sim \sqrt{E_0}, \quad (9)$$

so the oscillator strength of the lowest exciton grows like the square root of the exciton binding energy. This is illustrated in Fig. 1b, which shows a series of absorption spectra with values of E_0 ranging from 0.01 to 1.5. The peak height grows with E_0 ; as long as E_0 is less than about 0.5, the growth clearly follows a $E_0^{1/2}$ behavior. For larger values of E_0 , the growth somewhat slows down, in accordance with Eq. (8).

3. Linear-response TDDFT for periodic solids with a gap

Here and in the following, \mathbf{k} and \mathbf{q} will denote wave vectors in the first BZ, and \mathbf{G} will denote reciprocal lattice vectors. From now on, we shall work in atomic units ($e = m = \hbar = 4\pi\epsilon_0 = 1$).

3.1. Basic formalism and Casida equation for the optical absorption in solids

In the following, we will consider periodic solids with fixed nuclei within the Born-Oppenheimer approximation, i.e., there are no phonons or electron-phonon interactions. We assume that the temperature is zero and that there are no defects, impurities or surface effects. Furthermore, we will limit the discussion to nonmagnetic materials in which all spin-up and spin-down states are equally occupied, and we will only consider spin-independent quantities.

Under these circumstances, the linear density response to a scalar perturbing potential can be written as

$$n_{1\mathbf{G}}(\mathbf{k}, \omega) = \sum_{\mathbf{G}'} \chi_{\mathbf{G}\mathbf{G}'}(\mathbf{k}, \omega) v_{1\mathbf{G}'}(\mathbf{k}, \omega), \quad (10)$$

where $n_{1\mathbf{G}}(\mathbf{k}, \omega)$ is the density response in reciprocal space, $v_{1\mathbf{G}'}(\mathbf{k}, \omega)$ is the perturbing potential, and $\chi_{\mathbf{G}\mathbf{G}'}(\mathbf{k}, \omega)$ is the density-density response function of the system, including electron-electron interactions.

In TDDFT, the full interacting density-density response function in a lattice periodic system is given, in principle exactly, by

$$\chi_{\mathbf{G}\mathbf{G}'}(\mathbf{k}, \omega) = \chi_{\mathbf{G}\mathbf{G}'}^{\text{KS}}(\mathbf{k}, \omega) + \sum_{\mathbf{G}_1, \mathbf{G}_2} \chi_{\mathbf{G}\mathbf{G}_1}^{\text{KS}}(\mathbf{k}, \omega) f_{\mathbf{G}_1\mathbf{G}_2}^{\text{Hxc}}(\mathbf{k}, \omega) \chi_{\mathbf{G}_2\mathbf{G}'}(\mathbf{k}, \omega). \quad (11)$$

Here, the Kohn-Sham response function is

$$\chi_{\mathbf{G}\mathbf{G}'}^{\text{KS}}(\mathbf{k}, \omega) = \frac{2}{\mathcal{V}} \sum_{\mathbf{k}' \in \text{BZ}} \sum_{j, l=1}^{\infty} \frac{f_{j\mathbf{k}'} - f_{l\mathbf{k}+\mathbf{k}'}}{\omega + \varepsilon_{j\mathbf{k}'} - \varepsilon_{l\mathbf{k}+\mathbf{k}'} + i\eta}$$

$$\times \int_{\text{cell}} d\mathbf{r} \varphi_{j\mathbf{k}'}^*(\mathbf{r}) e^{-i(\mathbf{k}+\mathbf{G})\cdot\mathbf{r}} \varphi_{l\mathbf{k}+\mathbf{k}'}(\mathbf{r}) \int_{\text{cell}} d\mathbf{r}' \varphi_{l\mathbf{k}+\mathbf{k}'}^*(\mathbf{r}') e^{i(\mathbf{k}+\mathbf{G}')\cdot\mathbf{r}'} \varphi_{j\mathbf{k}'}(\mathbf{r}'), \quad (12)$$

where \mathcal{V} is the volume of the unit cell. To construct $\chi_{\mathbf{G}\mathbf{G}'}^{\text{KS}}(\mathbf{k}, \omega)$, we need the Kohn-Sham band structure, that is, the Kohn-Sham single-particle Bloch functions $\varphi_{j\mathbf{k}}(\mathbf{r})$ and energy eigenvalues $\varepsilon_{j\mathbf{k}}$, where j is the band index. The second sum in Eq. (12) runs over all occupied and unoccupied bands, where $f_{j\mathbf{k}}$ is an occupation factor (1 if the state $\varphi_{j\mathbf{k}}$ is occupied, 0 if empty). In the following, we will use a bra-ket notation to abbreviate the integrals over the unit cell, so that

$$\begin{aligned} \chi_{\mathbf{G}\mathbf{G}'}^{\text{KS}}(\mathbf{k}, \omega) &= \frac{2}{\mathcal{V}} \sum_{\mathbf{k}' \in \text{BZ}} \sum_{j,l=1}^{\infty} \frac{f_{j\mathbf{k}'} - f_{l\mathbf{k}+\mathbf{k}'}}{\omega + \varepsilon_{j\mathbf{k}'} - \varepsilon_{l\mathbf{k}+\mathbf{k}'} + i\eta} \\ &\times \langle j\mathbf{k}' | e^{-i(\mathbf{k}+\mathbf{G})\cdot\mathbf{r}} | l\mathbf{k} + \mathbf{k}' \rangle \langle l\mathbf{k} + \mathbf{k}' | e^{i(\mathbf{k}+\mathbf{G}')\cdot\mathbf{r}'} | j\mathbf{k}' \rangle, \end{aligned} \quad (13)$$

where \mathbf{r} and \mathbf{r}' in the exponents are understood to be integrated over.

Equation (11) for the full response function has the form of a Dyson equation, featuring the Hartree-xc kernel

$$f_{\mathbf{G}\mathbf{G}'}^{\text{Hxc}}(\mathbf{k}, \omega) = \frac{4\pi\delta_{\mathbf{G}\mathbf{G}'}}{|\mathbf{k} + \mathbf{G}|^2} + f_{\mathbf{G}\mathbf{G}'}^{\text{xc}}(\mathbf{k}, \omega), \quad (14)$$

where the first term on the right-hand side is the Hartree kernel $f_{\mathbf{G}\mathbf{G}'}^{\text{H}}(\mathbf{k})$, which is diagonal in \mathbf{G}, \mathbf{G}' and independent of frequency. The xc kernel $f_{\mathbf{G}\mathbf{G}'}^{\text{xc}}(\mathbf{k}, \omega)$ will be the subject of further discussion below.

Combining Eqs. (10) and (11), the density response is given within TDDFT as

$$n_{1\mathbf{G}}(\mathbf{k}, \omega) = \sum_{\mathbf{G}'} \chi_{\mathbf{G}\mathbf{G}'}^{\text{KS}}(\mathbf{k}, \omega) \left[v_{1\mathbf{G}'}(\mathbf{k}, \omega) + \sum_{\mathbf{G}''} f_{\mathbf{G}'\mathbf{G}''}^{\text{Hxc}}(\mathbf{k}, \omega) n_{1\mathbf{G}''}(\mathbf{k}, \omega) \right]. \quad (15)$$

The standard approach in TDDFT to calculate excitation energies from the linear-response formalism is known as the Casida equation [37]. The idea is to set the perturbation to zero and look for self-sustained solutions to the density response equation which correspond to “eigenmodes” of the density, oscillating with characteristic frequencies: these are the excitation energies of the system [10].

The Casida approach is very widely used for finite systems such as molecules or clusters. For the case of periodic systems, there are additional points to consider. We start from Eq. (15), which is in principle exact. Now let us consider two phenomena which are important in materials, namely electron energy loss and optical absorption. These two effects differ from each other in the following ways [2, 5]:

- The *loss function* is related to the imaginary part of the density-density response function associated with the response to a *microscopic external scalar potential* (for example, caused by a charged projectile passing through the system). In loss spectra one can observe *plasmons*. To calculate electron loss spectra using the Casida approach amounts to setting $v_{1\mathbf{G}'}(\mathbf{k}, \omega) = 0$ in Eq. (15).

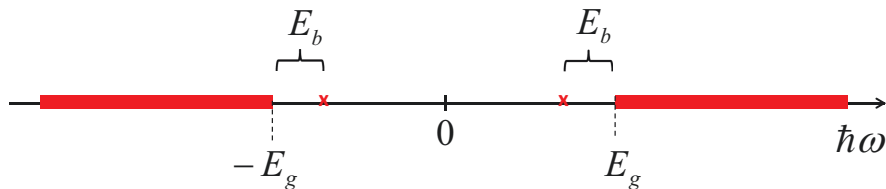


Figure 2. Schematic illustration of the distribution of excitation energies from the solution of the Casida equation. E_g is the Kohn-Sham band gap, and E_b is the exciton binding energy.

- The *optical absorption* measures the response to the *total macroscopic classical perturbation*, which includes the external scalar potential (in dipole approximation) associated with the electromagnetic wave, and the macroscopic classical induced field. In absorption spectra one can observe *excitons*. To calculate optical absorption spectra from the Casida equation, one needs to set $v_{1\mathbf{G}'}(\mathbf{k}, \omega) + f_{00}^H n_{10}(\mathbf{k}, \omega) = 0$ in Eq. (15). Thus, in the Casida equation the $\mathbf{G} = 0$ part of the Hartree kernel must be removed.

The derivation of the Casida equation for optical absorption in periodic solids proceeds along similar lines as for finite systems [10]. As shown in Appendix A, one can recast Eq. (15) into

$$\sum_{\mathbf{k}'j\mathbf{b}} \left\{ [(\varepsilon_{a\mathbf{k}} - \varepsilon_{i\mathbf{k}})\delta_{ji}\delta_{ba}\delta_{\mathbf{k}\mathbf{k}'} + K_{iak,jb\mathbf{k}'}] X_{jb\mathbf{k}'} + K_{iak,bj\mathbf{k}'} Y_{jb\mathbf{k}'} \right\} = -\omega X_{ia\mathbf{k}} \quad (16)$$

$$\sum_{\mathbf{k}'j\mathbf{b}} \left\{ K_{ai\mathbf{k},jb\mathbf{k}'} X_{jb\mathbf{k}'} + [(\varepsilon_{a\mathbf{k}} - \varepsilon_{i\mathbf{k}})\delta_{ba}\delta_{ji}\delta_{\mathbf{k}\mathbf{k}'} + K_{ai\mathbf{k},bj\mathbf{k}'}] Y_{jb\mathbf{k}'} \right\} = \omega Y_{ia\mathbf{k}}, \quad (17)$$

which has the form of a (nonhermitian) eigenvalue problem. Here, i, j and a, b are indices which run over occupied and unoccupied bands, respectively. Thus, $\varepsilon_{a\mathbf{k}} - \varepsilon_{i\mathbf{k}}$ are single-particle transitions with no momentum transfer (vertical Kohn-Sham excitation energies). The coupling matrix elements are given by

$$K_{iak,jb\mathbf{k}'}(\omega) = \lim_{\mathbf{q} \rightarrow 0} \frac{2}{\mathcal{V}} \sum_{\mathbf{G}\mathbf{G}'} \langle i\mathbf{k} | e^{i(\mathbf{q}+\mathbf{G})\cdot\mathbf{r}} | a\mathbf{k} \rangle \langle b\mathbf{k}' | e^{-i(\mathbf{q}+\mathbf{G}')\cdot\mathbf{r}} | j\mathbf{k}' \rangle \times \left(\frac{4\pi\delta_{\mathbf{G}\mathbf{G}'}}{|\mathbf{q} + \mathbf{G}|^2} (1 - \delta_{\mathbf{G},0}) + f_{\mathbf{G}\mathbf{G}'}^{\text{xc}}(\mathbf{q}, \omega) \right). \quad (18)$$

Here, the limit $\mathbf{q} \rightarrow 0$ indicates that we are considering the optical limits of vertical excitations in momentum space. Furthermore, the xc kernel is in principle dependent on the frequency ω , which would make the Casida equation a nonlinear eigenvalue problem. In practice, this ω -dependence is almost always ignored, i.e., one makes the adiabatic approximation.

The solution (i.e., the spectrum of eigenvalues) of the Casida equation (16), (17) provides us with the excitation energies of the system. The distribution of excitation energies is schematically illustrated in Fig. 2, assuming a frequency-independent xc

kernel. There is a continuum of excitation energies starting at the Kohn-Sham band gap E_g , shown as a broad red line. Excitons appear as isolated frequencies at energies below the band gap. The distance between such isolated excitation energies and the onset of the continuum is the exciton binding energy E_b . We here assume that only a single bound exciton is present [57].

Notice further that the distribution of excitation energies has mirror symmetry around zero. In other words, for every excitation energy ω_0 there is a counterpart at $-\omega_0$. This follows directly from the structure of the Casida equation (16), (17), and can be viewed in the sense that every excitation comes with its corresponding de-excitation.

From the eigenvectors $X_{iak}^{(m)}, Y_{iak}^{(m)}$ we can construct the density response which corresponds to a given excitation energy ω_m :

$$n_{1\mathbf{G}}(\omega_m) = \frac{2}{V} \sum_{\mathbf{k}} \sum_{jb} \left\{ \langle b\mathbf{k} | e^{-i\mathbf{G}\cdot\mathbf{r}} | j\mathbf{k}' \rangle X_{jb\mathbf{k}}^{(m)} + \langle j\mathbf{k} | e^{-i\mathbf{G}\cdot\mathbf{r}} | b\mathbf{k}' \rangle Y_{jb\mathbf{k}}^{(m)} \right\}. \quad (19)$$

The density response of the eigenmodes is lattice periodic, so we see that $n_{1\mathbf{G}}(\omega_n)$ only depends on reciprocal lattice vectors. Transforming this back into real space gives

$$n_1(\mathbf{r}, \omega_m) = 2 \sum_{\mathbf{k}jb} \left\{ X_{jb\mathbf{k}}^{(m)} \varphi_{b\mathbf{k}}^*(\mathbf{r}) \varphi_{j\mathbf{k}}(\mathbf{r}) + Y_{jb\mathbf{k}}^{(m)} \varphi_{j\mathbf{k}}^*(\mathbf{r}) \varphi_{b\mathbf{k}}(\mathbf{r}) \right\}. \quad (20)$$

3.2. Constructing the macroscopic dielectric function

As we discussed above, the quantity of interest for excitons is the macroscopic dielectric function $\epsilon_{\text{mac}}(\omega)$, whose imaginary part determines the optical absorption in materials.

The *microscopic* dielectric function for lattice-periodic systems is defined as [5]

$$\epsilon_{\mathbf{G}\mathbf{G}'}(\mathbf{k}, \omega) = \delta_{\mathbf{G}\mathbf{G}'} - v_{\mathbf{G}}(\mathbf{k}) \tilde{\chi}_{\mathbf{G}\mathbf{G}'}(\mathbf{k}, \omega), \quad (21)$$

where $v_{\mathbf{G}}(\mathbf{k}) = 4\pi/|\mathbf{k} + \mathbf{G}|^2$ and $\tilde{\chi}$ is the so-called proper response function, which obeys a Dyson equation similar to Eq. (11), but using only $f_{\mathbf{G}_1\mathbf{G}_2}^{\text{xc}}$ instead of $f_{\mathbf{G}_1\mathbf{G}_2}^{\text{Hxc}}$. Naively, one might think that $\epsilon_{\text{mac}}(\omega)$ simply follows from $\epsilon_{\mathbf{G}\mathbf{G}'}(\mathbf{k}, \omega)$ by setting \mathbf{G}, \mathbf{G}' and \mathbf{k} to zero. However, the macroscopic limit is more subtle, and turns out to be given by [58,59]

$$\epsilon_{\text{mac}}(\omega) = \lim_{k \rightarrow 0} \left[\epsilon_{\mathbf{G}\mathbf{G}'}^{-1}(\mathbf{k}, \omega) \Big|_{\substack{\mathbf{G}=0 \\ \mathbf{G}'=0}} \right]^{-1}. \quad (22)$$

This expression is valid for crystals with cubic symmetry (the non-cubic case is more complicated [60]). In other words, $\epsilon_{\text{mac}}(\omega)$ emerges as the inverse of the inverse dielectric function; this is so because local-field effects contribute to the macroscopic limit. The matrix algebra in Eq. (22) can be worked out [2,10], and one finds that the macroscopic dielectric function can be obtained from linear-response TDDFT as follows:

$$\epsilon_{\text{mac}}(\omega) = 1 - \lim_{k \rightarrow 0} v(\mathbf{k}) \bar{\chi}_{00}(\mathbf{k}, \omega), \quad (23)$$

where $\bar{\chi}_{\mathbf{G}\mathbf{G}'}(\mathbf{k}, \omega)$ is the full response function calculated with the modified Hartree kernel $\bar{f}_{\mathbf{G}\mathbf{G}'}^{\text{H}}(\mathbf{k}) = 4\pi\delta_{\mathbf{G}\mathbf{G}'}(1 - \delta_{\mathbf{G},0})/|\mathbf{k} + \mathbf{G}|^2$ (which excludes the $\mathbf{G} = 0$ term), and $v(\mathbf{k}) = 4\pi/k^2$.

There are two ways in which the full response function $\bar{\chi}_{\mathbf{G}\mathbf{G}'}(\mathbf{k}, \omega)$ can be obtained from linear-response TDDFT. The first is by direct solution of the TDDFT Dyson equation (11), which formally requires the solution of a matrix equation whose dimension is the number of reciprocal lattice vectors \mathbf{G} ; it also requires the construction of the Kohn-Sham response function $\chi_{\mathbf{G}\mathbf{G}'}^{\text{KS}}(\mathbf{k}, \omega)$, which involves a summation over occupied and empty bands and over \mathbf{k} -points within the BZ, see Eq. (12).

The second way to obtain $\bar{\chi}_{\mathbf{G}\mathbf{G}'}(\mathbf{k}, \omega)$ is from the solutions of the Casida equation, which is a (nonhermitian) eigenvalue equation whose dimension is twice the number of \mathbf{k} -points times the numbers of occupied and unoccupied bands, which is typically much larger than the dimension of the Dyson matrix equation (see above). It is possible to reduce the dimension of the Casida equation by half, exploiting time-reversal symmetry [61], but we will not pursue this here.

Let us now discuss how the interacting response function follows from the Casida equation. Starting point is again the density response equation, Eq. (15). But now we do not set the external perturbation to zero, as we did earlier; however, as before, we set the long-range part of the Hartree kernel to zero, $f_{00}^{\text{H}} = 0$. We then repeat the earlier derivation, which eventually leads to the following generalized Casida equation:

$$\begin{aligned} & \sum_{\mathbf{k}'j\mathbf{b}} \left\{ [(\varepsilon_{a\mathbf{k}} - \varepsilon_{i\mathbf{q}+\mathbf{k}})\delta_{ji}\delta_{ba}\delta_{\mathbf{k}\mathbf{k}'} + K_{ia\mathbf{k},j\mathbf{b}\mathbf{k}'}^{\mathbf{q}}] X_{j\mathbf{b}\mathbf{k}'}^{\mathbf{q}\omega} + K_{ia\mathbf{k},j\mathbf{b}\mathbf{k}'}^{\mathbf{q}} Y_{j\mathbf{b}\mathbf{k}'}^{\mathbf{q}\omega} \right\} + \omega X_{ia\mathbf{k}}^{\mathbf{q}\omega} \\ & = -V_{ia\mathbf{k}}^{\mathbf{q}\omega} \end{aligned} \quad (24)$$

$$\begin{aligned} & \sum_{\mathbf{k}'j\mathbf{b}} \left\{ K_{ai\mathbf{k},j\mathbf{b}\mathbf{k}'}^{\mathbf{q}} X_{j\mathbf{b}\mathbf{k}'}^{\mathbf{q}\omega} + [(\varepsilon_{a\mathbf{q}+\mathbf{k}} - \varepsilon_{i\mathbf{k}})\delta_{ba}\delta_{ji}\delta_{\mathbf{k}\mathbf{k}'} + K_{ai\mathbf{k},j\mathbf{b}\mathbf{k}'}^{\mathbf{q}}] Y_{j\mathbf{b}\mathbf{k}'}^{\mathbf{q}\omega} \right\} - \omega Y_{ia\mathbf{k}}^{\mathbf{q}\omega} \\ & = -V_{ai\mathbf{k}}^{\mathbf{q}\omega}, \end{aligned} \quad (25)$$

where

$$V_{ia\mathbf{k}}^{\mathbf{q}\omega} = \sum_{\mathbf{G}} \langle i\mathbf{q} + \mathbf{k} | e^{i(\mathbf{q}+\mathbf{G})\cdot\mathbf{r}} | a\mathbf{k} \rangle v_{1\mathbf{G}}(\mathbf{q}, \omega) \quad (26)$$

and $K_{ai\mathbf{k},j\mathbf{b}\mathbf{k}'}^{\mathbf{q}}$ is defined as in Eq. (18), but without $\mathbf{q} \rightarrow 0$. Eqs. (24) and (25) are now no longer an eigenvalue problem, but a system of linear equations, with the solutions $X_{ia\mathbf{k}}^{\mathbf{q}\omega}, Y_{ia\mathbf{k}}^{\mathbf{q}\omega}$ parametrically depending on the wave vector \mathbf{q} and the frequency ω . From the solutions, one can construct the density response to the perturbation $v_{1\mathbf{G}}(\mathbf{q}, \omega)$ as

$$\begin{aligned} n_{1\mathbf{G}}(\mathbf{q}, \omega) = \frac{2}{\mathcal{V}} \sum_{\mathbf{k}ia} \left\{ \langle a\mathbf{k} | e^{-i(\mathbf{q}+\mathbf{G})\cdot\mathbf{r}} | i\mathbf{q} + \mathbf{k} \rangle X_{ia\mathbf{k}}^{\mathbf{q}\omega} \right. \\ \left. + \langle i\mathbf{k} | e^{-i(\mathbf{q}+\mathbf{G})\cdot\mathbf{r}} | a\mathbf{k} + \mathbf{k} \rangle Y_{ia\mathbf{k}}^{\mathbf{q}\omega} \right\}. \end{aligned} \quad (27)$$

The trick is now to choose a very special perturbation, namely,

$$v_{1\mathbf{G}}(\mathbf{q}, \omega) = \delta_{\mathbf{G}\mathbf{G}_0}, \quad (28)$$

where \mathbf{G}_0 is a certain fixed reciprocal lattice vector. From Eq. (10) we then immediately obtain

$$n_{1\mathbf{G}}(\mathbf{q}, \omega) = \chi_{\mathbf{G}\mathbf{G}_0}(\mathbf{q}, \omega). \quad (29)$$

For this special case, the matrix elements (26) of the perturbation become

$$V_{iak}^{\mathbf{q};\mathbf{G}_0} = \langle i\mathbf{q} + \mathbf{k} | e^{i(\mathbf{q}+\mathbf{G}_0)\cdot\mathbf{r}} | a\mathbf{k} \rangle \quad (30)$$

independent of frequency, but depending on \mathbf{G}_0 . The solutions will therefore depend on \mathbf{G}_0 as well: $X_{iak}^{\mathbf{q}\omega;\mathbf{G}_0}, Y_{iak}^{\mathbf{q}\omega;\mathbf{G}_0}$. The response function then follows as

$$\begin{aligned} \chi_{\mathbf{G}\mathbf{G}_0}(\mathbf{q}, \omega) = \frac{2}{\mathcal{V}} \sum_{kia} \left\{ \langle a\mathbf{k} | e^{-i(\mathbf{q}+\mathbf{G})\cdot\mathbf{r}} | i\mathbf{q} + \mathbf{k} \rangle X_{iak}^{\mathbf{q}\omega;\mathbf{G}_0} \right. \\ \left. + \langle i\mathbf{k} | e^{-i(\mathbf{q}+\mathbf{G})\cdot\mathbf{r}} | a\mathbf{q} + \mathbf{k} \rangle Y_{iak}^{\mathbf{q}\omega;\mathbf{G}_0} \right\}. \end{aligned} \quad (31)$$

So far so good; but constructing the full response function in this manner seems quite cumbersome, since it requires solving a Casida-like system of linear equations, Eqs. (24) and (25), for many different values of (\mathbf{q}, ω) . This can be elegantly avoided using a spectral representation.

In a spectral representation, the solution vectors (\mathbf{X}, \mathbf{Y}) of the Casida equation in the presence of an external frequency-dependent perturbation \mathbf{v} are expanded in the complete set of Casida eigenvectors (eigenmodes), calculated with $\mathbf{v} = 0$. Explicitly,

$$\begin{pmatrix} \mathbf{X} \\ \mathbf{Y} \end{pmatrix} = \sum_m \text{sign}(\omega_m) \begin{pmatrix} \mathbf{X}_m \\ \mathbf{Y}_m \end{pmatrix} \frac{\langle \mathbf{X}_m | \mathbf{v} \rangle + \langle \mathbf{Y}_m | \mathbf{v}^* \rangle}{\omega - \omega_m + i\eta}, \quad (32)$$

where ω_m is the m^{th} excitation energy, $(\mathbf{X}_m, \mathbf{Y}_m)$ the corresponding eigenvector, and the sum goes over both the positive and negative parts of the excitation spectrum, see Fig. 2.

Specifically, for the perturbation (28) we have

$$\langle \mathbf{X}_m | \mathbf{v} \rangle = \sum_{\mathbf{k}} \sum_{ia} X_{m,iak}^{\mathbf{q}*} \langle i\mathbf{q} + \mathbf{k} | e^{i(\mathbf{q}+\mathbf{G}_0)\cdot\mathbf{r}} | a\mathbf{k} \rangle \quad (33)$$

and similar for $\langle \mathbf{Y}_m | \mathbf{v}^* \rangle$, where the $(\mathbf{X}_m, \mathbf{Y}_m)$ carry a superscript \mathbf{q} , since we here consider the Casida equation (16), (17) for generally nonvertical excitations. Taken everything together, the final expression for the full response function is

$$\begin{aligned} \chi_{\mathbf{G}\mathbf{G}'}(\mathbf{q}, \omega) = \frac{2}{\mathcal{V}} \sum_m \frac{\text{sign}(\omega_m^{\mathbf{q}})}{\omega - \omega_m^{\mathbf{q}} + i\eta} \sum_{\mathbf{k}\mathbf{k}'} \sum_{ia,jb} \\ \times \left\{ \langle b\mathbf{k} | e^{-i(\mathbf{q}+\mathbf{G})\cdot\mathbf{r}} | j\mathbf{q} + \mathbf{k} \rangle X_{m,jbk}^{\mathbf{q}} X_{m,iak'}^{\mathbf{q}*} \langle i\mathbf{q} + \mathbf{k}' | e^{i(\mathbf{q}+\mathbf{G}')\cdot\mathbf{r}} | a\mathbf{k}' \rangle \right. \\ \left. + \langle j\mathbf{k} | e^{-i(\mathbf{q}+\mathbf{G})\cdot\mathbf{r}} | b\mathbf{q} + \mathbf{k} \rangle Y_{m,jbk}^{\mathbf{q}} Y_{m,iak'}^{\mathbf{q}*} \langle a\mathbf{q} + \mathbf{k}' | e^{i(\mathbf{q}+\mathbf{G}')\cdot\mathbf{r}} | i\mathbf{k}' \rangle \right\} \end{aligned} \quad (34)$$

We can now immediately obtain the macroscopic dielectric function (23):

$$\begin{aligned} \epsilon_{\text{mac}}(\omega) = 1 - \lim_{q \rightarrow 0} v(\mathbf{q}) \sum_m \frac{\text{sign}(\omega_m)}{\omega - \omega_m + i\eta} \\ \times \left\{ \left| \sum_{\mathbf{k}j\mathbf{b}} \langle b\mathbf{k} | e^{-i\mathbf{q}\cdot\mathbf{r}} | j\mathbf{k} \rangle X_{j\mathbf{b}\mathbf{k}}^{(m)} \right|^2 + \left| \sum_{\mathbf{k}j\mathbf{b}} \langle j\mathbf{k} | e^{-i\mathbf{q}\cdot\mathbf{r}} | b\mathbf{k} \rangle Y_{j\mathbf{b}\mathbf{k}}^{(m)} \right|^2 \right\}. \end{aligned} \quad (35)$$

With the above theoretical framework it is possible, at least in principle, to exactly calculate $\epsilon_{\text{mac}}(\omega)$ for any given material, provided the exact xc kernel is used. However,

it is already a tough mission to construct high-quality xc functionals for ground-state DFT, let alone finding the xc kernel f_{xc} via Eq. (1), in particular for periodic solids. Approximations will have to be made, which will be reviewed in the next section.

4. Overview of approximate xc kernels

4.1. Long-range behavior of the exact xc kernel and (semi)local approximations

The xc kernel in reciprocal space, $f_{\mathbf{G}\mathbf{G}'}^{\text{xc}}(\mathbf{q}, \omega)$, can be written as a matrix in the space of reciprocal lattice vectors \mathbf{G}, \mathbf{G}' :

$$\begin{aligned} \underline{\underline{f}}^{\text{xc}}(\mathbf{q}, \omega) &= \begin{pmatrix} f_{00}^{\text{xc}}(\mathbf{q}, \omega) & f_{01}^{\text{xc}}(\mathbf{q}, \omega) & f_{02}^{\text{xc}}(\mathbf{q}, \omega) & \dots \\ f_{10}^{\text{xc}}(\mathbf{q}, \omega) & f_{11}^{\text{xc}}(\mathbf{q}, \omega) & f_{12}^{\text{xc}}(\mathbf{q}, \omega) & \dots \\ f_{20}^{\text{xc}}(\mathbf{q}, \omega) & f_{21}^{\text{xc}}(\mathbf{q}, \omega) & f_{22}^{\text{xc}}(\mathbf{q}, \omega) & \dots \\ \vdots & \vdots & \vdots & \ddots \end{pmatrix} \\ &= \begin{pmatrix} \text{head} & \text{wing} \\ \text{wing} & \text{body} \end{pmatrix}, \end{aligned} \quad (36)$$

where the subscripts are labels enumerating the reciprocal lattice vectors, and the dashed lines demarcate different regions of the matrix. Specifically, the subscript 00 means that $\mathbf{G} = \mathbf{0}$ and $\mathbf{G}' = \mathbf{0}$, which is called the “head” of the matrix. The “wings” of the matrix are those elements where $\mathbf{G} = \mathbf{0}$ and \mathbf{G}' is nonvanishing (01, 02, ...), or vice versa (10, 20, ...). The remaining elements of $f_{\mathbf{G}\mathbf{G}'}^{\text{xc}}(\mathbf{q}, \omega)$, where both \mathbf{G} and \mathbf{G}' are nonvanishing, constitute the “body” of the matrix.

As pointed out after Eq. (18), for optical excitations the limit $\mathbf{q} \rightarrow 0$ of the xc kernel is needed. The analytic form of the small- \mathbf{q} limit is known to have the following form [62–64]:

$$\lim_{\mathbf{q} \rightarrow 0} \underline{\underline{f}}^{\text{xc}}(\mathbf{q}, \omega) = \begin{pmatrix} \frac{\kappa_{00}}{q^2} & \frac{\kappa_{01}}{q} & \frac{\kappa_{02}}{q} & \dots \\ \frac{\kappa_{10}}{q} & \kappa_{11} & \kappa_{12} & \dots \\ \frac{\kappa_{20}}{q} & \kappa_{21} & \kappa_{22} & \dots \\ \vdots & \vdots & \vdots & \ddots \end{pmatrix}, \quad (37)$$

where the coefficients κ_{ij} are independent of \mathbf{q} but may in general be ω -dependent; formally, they are functionals of the ground-state density n_0 . Thus, the head of $\underline{\underline{f}}^{\text{xc}}$ diverges as q^{-2} , the wing elements diverge as q^{-1} , and the body elements are q -independent (to leading order) as $\mathbf{q} \rightarrow 0$.

The coupling matrix (18) involves a sum over \mathbf{G}, \mathbf{G}' of the Hartree and xc kernels, weighted with the matrix elements $\langle i\mathbf{k}|e^{i(\mathbf{q}+\mathbf{G})\cdot\mathbf{r}}|a\mathbf{k}\rangle\langle b\mathbf{k}'|e^{-i(\mathbf{q}+\mathbf{G}')\cdot\mathbf{r}}|j\mathbf{k}'\rangle$. For $\mathbf{G} = \mathbf{0}$, the matrix element $\langle i\mathbf{k}|e^{i(\mathbf{q}+\mathbf{G})\cdot\mathbf{r}}|a\mathbf{k}\rangle$ vanishes linearly in \mathbf{q} when $\mathbf{q} \rightarrow 0$; more precisely [65],

$$\lim_{\mathbf{q} \rightarrow 0} \langle i\mathbf{k}|e^{i\mathbf{q}\cdot\mathbf{r}}|a\mathbf{k}\rangle = \mathbf{q} \cdot \frac{\langle i\mathbf{k}|\mathbf{p}|a\mathbf{k}\rangle}{\varepsilon_{i\mathbf{k}} - \varepsilon_{a\mathbf{k}}}, \quad (38)$$

where \mathbf{p} is the momentum operator, and similarly for the other matrix element, $\langle b\mathbf{k}' | e^{-i(\mathbf{q}+\mathbf{G}')\cdot\mathbf{r}} | j\mathbf{k}' \rangle$. This means that the head contribution ($\mathbf{G} = \mathbf{G}' = 0$) to $K_{ia\mathbf{k},jb\mathbf{k}'}^{\text{xc}}$ will remain finite since $f_{00}^{\text{xc}}(\mathbf{q})$ diverges as q^{-2} , as we have seen above. Likewise, the wing contributions ($\mathbf{G} = 0$ and \mathbf{G}' finite, and vice versa) remain finite since the wings of the xc kernel diverge at as q^{-1} . The body contributions to $K_{ia\mathbf{k},jb\mathbf{k}'}^{\text{xc}}$ are nonvanishing as well, but in general make smaller contributions than head and wings, especially for large \mathbf{G} and \mathbf{G}' .

Thus, we see that the small- \mathbf{q} limit of the xc kernel matrix, especially the q^{-2} divergence of the head, is crucial to capture the optical properties close to the band gap correctly. Since $\mathbf{q} \rightarrow 0$ corresponds to $|\mathbf{r} - \mathbf{r}'| \rightarrow \infty$, this divergence in \mathbf{q} -space implies a spatially long-range behavior of the xc kernel of the type $1/|\mathbf{r} - \mathbf{r}'|$.

By contrast, all local and semilocal xc kernels (ALDA and AGGAs) remain finite for all \mathbf{G} , \mathbf{G}' and \mathbf{q} . As a case in point, consider the ALDA xc kernel, whose real-space form is

$$f_{\text{xc}}^{\text{ALDA}}(\mathbf{r}, \mathbf{r}') = \left. \frac{d^2 e_{\text{xc}}(n)}{dn^2} \right|_{n=n_0(\mathbf{r})} \delta(\mathbf{r} - \mathbf{r}'), \quad (39)$$

where $e_{\text{xc}}(n)$ is the xc energy density of a homogeneous electron gas of uniform density n and $n_0(\mathbf{r})$ is the actual ground-state density of the system. The \mathbf{q} -dependence of the Fourier transformed ALDA kernel simply drops out [66]:

$$f_{\text{xc},\mathbf{G}\mathbf{G}'}^{\text{ALDA}}(\mathbf{q}) = \frac{1}{\mathcal{V}} \int_{\text{cell}} d\mathbf{r} e^{-i(\mathbf{G}-\mathbf{G}')\cdot\mathbf{r}} \left. \frac{d^2 e_{\text{xc}}(n)}{dn^2} \right|_{n=n_0(\mathbf{r})}. \quad (40)$$

If $f_{\text{xc},\mathbf{G}\mathbf{G}'}^{\text{ALDA}}(\mathbf{q})$ is substituted into Eq. (18), then the contributions from the head and wings of f_{xc} to $K_{ia\mathbf{k},jb\mathbf{k}'}^{\text{xc}}$ will vanish, which only leaves body contributions, but these are very weak. As a result, no excitonic binding is produced. The AGGA xc kernels behave in a similar fashion. An even more extreme example is the contact xc kernel, whose real- and reciprocal-space forms are

$$f_{\text{xc}}^{\text{cont}}(\mathbf{r}, \mathbf{r}') = -A_{\text{cont}} \delta(\mathbf{r} - \mathbf{r}'), \quad f_{\text{xc},\mathbf{G}\mathbf{G}'}^{\text{cont}}(\mathbf{q}) = -A_{\text{cont}} \delta_{\mathbf{G}\mathbf{G}'}, \quad (41)$$


where A_{cont} is a positive constant. The contact xc kernel is diagonal in \mathbf{G} , \mathbf{G}' and \mathbf{q} -independent. After what was said, it may come as a big surprise that ultra-short-range xc kernels such as $f_{\text{xc}}^{\text{cont}}$ can actually lead to bound excitons, if the constant A_{cont} is properly chosen [38, 44, 57]. Likewise, a scaled ALDA, $\alpha f_{\text{xc},\mathbf{G}\mathbf{G}'}^{\text{ALDA}}$, would be capable of producing excitons, although the scaling factor α would have to be quite large (typically of order $\sim 10^3$). How is this possible? The answer lies in the local-field effects.

As we have seen, for ALDA and AGGA xc kernels, the head and wings cannot affect the optical spectrum, even after scaling with a large α ; similarly for the contact xc kernel (which doesn't even have wings). Thus, the only remaining possibility is through the body contributions to the coupling matrix $K_{ia\mathbf{k},jb\mathbf{k}'}^{\text{xc}}$. This means that the missing long-range behavior must be compensated by ultrastrong short-range electron-hole interactions, which dominate the repulsive Hartree kernel and lead to electron-hole attraction. It turns out [38, 43] that the contact xc kernel can be tuned to reproduce

certain features of the optical spectrum (for instance, a bound excitonic peak at the right position) but at the cost of a poor description of other parts of the spectrum. Thus, short-range excitonic kernels may be conceptually interesting but are of limited usefulness in practice.

4.2. Kernels from many-body theory

4.2.1. The exact-exchange kernel The frequency-dependent xc kernel can be formally constructed from many-body perturbation theory, using a diagrammatic expansion [67, 68]. The first-order term of this expansion is the exact exchange kernel $f_x(\mathbf{r}, \mathbf{r}', \omega)$, which can be represented as the sum of five diagrams:

$$\int d\mathbf{r}_1 \int d\mathbf{r}_2 \chi_{\text{KS}}(\mathbf{r}, \mathbf{r}_1, \omega) f_x(\mathbf{r}_1, \mathbf{r}_2, \omega) \chi_{\text{KS}}(\mathbf{r}_2, \mathbf{r}', \omega) =$$

(42)

Here, v_x is the exact exchange potential of DFT, which is defined as an orbital functional via the optimized effective potential (OEP) method [69, 70], and χ_{KS} is the noninteracting Kohn-Sham response functions using the orbitals obtained with v_x . Explicit expressions for these diagrams were given by Hellgren and von Barth [71, 72]. Alternatively, the exact exchange kernel can also be directly derived as the functional derivative $f_x(\omega) = \delta v_x(\omega) / \delta n(\omega)$ [73–75].

Kim and Görling [63] showed that the exact-exchange kernel (42) has the long-range behavior (37) that is necessary for the formation of excitons in periodic insulators. However, the electron–hole interaction in exact-exchange TDDFT turns out to be unscreened, which leads to a dramatic overbinding of the excitons. This can cause the exciton binding energy to be larger than the band gap, which leads to a collapse of the optical spectrum. To prevent this spectral collapse, the Coulomb interaction has to be screened [38, 76]. The effects of screening can be mimicked within exact-exchange TDDFT through a reciprocal-space cutoff of the Coulomb singularity [63, 77].

4.2.2. The “nanoquanta” kernel In general, Kohn-Sham band structures, even if calculated with the exact xc potential, have gaps that disagree with the exact quasiparticle gaps. To produce the correct onset of optical absorption, the xc kernel $f_{\mathbf{G}\mathbf{G}'}^{\text{xc}}(\mathbf{q}, \omega)$ has to fulfill two important and challenging tasks: it has to correct the gap and shift the Kohn–Sham band edge to the true quasiparticle band edge, and it has to give rise to the effective electron–hole attraction that is needed for excitonic features in the spectrum. Formally, the xc kernel can be separated into two parts [42, 43, 48],

$$f_{\text{xc}} = f_{\text{xc}}^{\text{qp}} + f_{\text{xc}}^{\text{ex}}. \quad (43)$$

The two parts, $f_{\text{xc}}^{\text{qp}}$ and $f_{\text{xc}}^{\text{ex}}$, are responsible for the opening of the gap and the excitonic effects, respectively, and they can be approximated separately.

Let us introduce the *proper* response function $\tilde{\chi}$ through the following Dyson-type equation:

$$\tilde{\chi} = \chi_{\text{KS}} + \chi_{\text{KS}} f_{\text{xc}} \tilde{\chi}, \quad (44)$$

where we use a shorthand notation that omits arguments and integrals. It is then easy to write down the following relations for the two parts of f_{xc} [48]:

$$\chi_{\text{qp}} = \chi_{\text{KS}} + \chi_{\text{KS}} f_{\text{xc}}^{\text{qp}} \chi_{\text{qp}}, \quad (45)$$

$$\tilde{\chi} = \chi_{\text{qp}} + \chi_{\text{qp}} f_{\text{xc}}^{\text{ex}} \tilde{\chi}. \quad (46)$$

Here, χ_{qp} is formally defined as the response function of the noninteracting quasiparticle system, which has the correct quasiparticle gap. To construct it from the Kohn-Sham band structure via Eq. (45), the quasiparticle xc kernel $f_{\text{xc}}^{\text{qp}}$ is needed. In the second step, the optical spectrum, including excitons, is then obtained from Eq. (46).

The first step of this two-step approach is almost always skipped in TDDFT, and the quasiparticle band structure (and hence χ_{qp}) is directly calculated without invoking $f_{\text{xc}}^{\text{qp}}$. This can be done with various techniques such as the *GW* approach, generalized Kohn-Sham schemes using hybrid functionals, or a straightforward correction of the Kohn-Sham band structure which opens up the gap using the so-called scissors operator. Very recently, Cavo *et al.* [78] proposed to relate the quasiparticle gap correction to the derivative discontinuity of ground-state DFT, which they approximate using an explicit expression in terms of Kohn-Sham ground-state quantities [79–81].

The next step is then to construct an approximation for $f_{\text{xc}}^{\text{ex}}$ from Eq. (46). To do this, we first replace $\chi_{\text{qp}} f_{\text{xc}}^{\text{ex}} \tilde{\chi} \approx \chi_{\text{qp}} f_{\text{xc}}^{\text{ex}} \chi_{\text{qp}}$. Next, we find a diagrammatic representation of $\tilde{\chi} - \chi_{\text{qp}}$. It turns out [3, 10, 38] that this can be accomplished by comparison with the BSE [2], which can be brought to a form that is analogous to Eq. (46), involving a suitable contraction of two-particle Green’s functions and four-point vertex functions. This diagrammatic representation leads to the following expression:

$$\begin{aligned} & \int d3 \int d4 \chi_{\text{qp}}(1, 3) f_{\text{xc}}^{\text{ex}}(3, 4) \chi_{\text{qp}}(4, 2) = \\ & \int d3 \int d4 G_{\text{qp}}(1, 3) G_{\text{qp}}(4, 1) W(3, 4) G_{\text{qp}}(3, 2) G_{\text{qp}}(2, 4), \end{aligned} \quad (47)$$

where the numbers represent space-time arguments, e.g., $1 = (\mathbf{r}_1, t_1)$. Equation (47) defines the xc kernel of Reining *et al.* [42] and many others (also known as the “nanoquanta” kernel). Here, G_{qp} is a quasiparticle Green’s function, and W is a screened interaction, formally defined as

$$W(1, 2) = w(1, 2) + \int d3 \int d4 w(1, 3) \chi_{\text{qp}}(3, 4) W(4, 2), \quad (48)$$

where $w(1, 2)$ is the bare Coulomb interaction.

The excitonic xc kernel $f_{\text{xc}}^{\text{ex}}$ of Eq. (47) has been tested in a variety of systems, and has been shown to perform in close agreement with the full BSE [2, 42, 43, 45, 47, 76, 82]. Unfortunately, the many-body xc kernel (47) is not simple to implement and computationally essentially as expensive as the BSE.

4.3. Long-range corrected kernels

In Section 3.1, we discussed the long-range behavior of the exact xc kernel, see Eq. (37). If we now boldly assume that these long-range effects dominate all other xc contributions—which is rather well justified for the case of weakly bound excitons in semiconductors—then we can simply approximate the xc kernel by its long-range form. The only remaining problem is to find suitable expressions for the coefficients κ_{ij} of the xc kernel matrix (37).

The first such approximation was put forward by Reining *et al.* [42], and has become known as the long-range corrected (LRC) kernel:

$$f_{\text{xc},\mathbf{G}\mathbf{G}'}^{\text{LRC}}(\mathbf{q}) = -\frac{\alpha}{|\mathbf{q} + \mathbf{G}|^2} \delta_{\mathbf{G}\mathbf{G}'}, \quad (49)$$

where α is an empirical parameter. In Ref. [42], the choice of $\alpha = 0.2$ led to a good description of the continuum excitons for silicon. In a more detailed follow-up study, Botti *et al.* [49] pointed out that a single value of α can, in general, only reproduce parts of the optical spectrum. Using a fit of the continuum parts of the optical spectra for a few materials, the following relation was suggested [49]:

$$\alpha = 4.651\epsilon_{\infty}^{-1} - 0.213. \quad (50)$$

The xc kernel thus becomes roughly proportional to the inverse dielectric constant ϵ_{∞}^{-1} , which makes sense since the construction of the nanoquanta xc kernel, Eq. (47), shows that matrix elements of the xc kernel are directly related to matrix elements of the screened Coulomb interaction.

A frequency-dependent form of the LRC kernel was proposed in Ref. [50],

$$f_{\text{xc},\mathbf{G}\mathbf{G}'}^{\text{LRC}}(\mathbf{q}, \omega) = -\frac{\alpha + \beta\omega^2}{|\mathbf{q} + \mathbf{G}|^2} \delta_{\mathbf{G}\mathbf{G}'}, \quad (51)$$

which led to some improvement over the static kernel (49). A recent study [83], however, showed that the frequency dependence of the xc kernel is, in general, more complicated than the quadratic dependence assumed in Eq. (51).

The LRC kernel demonstrates that it is possible to capture the essential excitonic physics of a broad range of materials in a very simple manner. However, empirical input is required in the form of the parameter α . In the following, we will discuss approximate xc kernels which have the same dominating long-range behavior as the LRC kernel, but do not depend on empirical fitting parameters.

4.4. The “bootstrap” kernel

Let us begin by deriving an exact expression for the xc kernel, starting from the Dyson-like equation for the full response function, Eq. (11), which we symbolically write as

$$\chi = \chi_{\text{KS}} + \chi_{\text{KS}} f_{\text{Hxc}} \chi, \quad (52)$$

where the Hartree kernel $f_{\text{H}} = v$ is just the bare Coulomb interaction v . Hence, the xc kernel becomes

$$f_{\text{xc}} = \frac{1}{\chi_{\text{KS}}} - \frac{1}{\chi} - v, \quad (53)$$

where we treat operators as numbers, i.e., we represent a matrix inverse simply as an algebraic inverse. Combining Eqs. (52) and (53), we get

$$f_{\text{xc}} = \frac{1 - v\chi_{\text{KS}}}{\chi_{\text{KS}}} - \frac{1 - f_{\text{Hxc}}\chi_{\text{KS}}}{\chi_{\text{KS}}}. \quad (54)$$

Now let us introduce the so-called proper response function $\tilde{\chi}$, defined similar to Eq. (53) as $\tilde{\chi} = \chi_{\text{KS}} + \chi_{\text{KS}}f_{\text{xc}}\tilde{\chi}$. In terms of the proper response function, the dielectric function is given by $\varepsilon = 1 - v\tilde{\chi}$, and it is not difficult to show that one gets

$$\varepsilon = \frac{1 - f_{\text{Hxc}}\chi_{\text{KS}}}{1 - f_{\text{xc}}\chi_{\text{KS}}}. \quad (55)$$

If we substitute this into Eq. (54), we get the following expression for the xc kernel:

$$f_{\text{xc}} = \frac{\varepsilon_{\text{RPA}}}{\chi_{\text{KS}}} - \frac{\varepsilon(1 - f_{\text{xc}}\chi_{\text{KS}})}{\chi_{\text{KS}}}, \quad (56)$$

where the dielectric function within the random phase approximation (RPA) is defined as $\varepsilon_{\text{RPA}} = 1 - v\chi_{\text{KS}}$. Solving Eq. (56) for f_{xc} finally gives

$$f_{\text{xc}} = \frac{\varepsilon - \varepsilon_{\text{RPA}}}{(\varepsilon - 1)\chi_{\text{KS}}}. \quad (57)$$

The purpose of this exercise is to show that the xc kernel can be formally written entirely in terms of the inverse Kohn-Sham response function combined with the full and RPA dielectric functions. So far, everything has been exact, keeping in mind that all quantities in Eq. (57) are matrices in \mathbf{G}, \mathbf{G}' .

Expression (57) shows immediately that the head of the xc kernel, $f_{00}^{\text{xc}}(\mathbf{q}, \omega)$, behaves as q^{-2} , since the head of χ_{KS} goes as q^2 and the heads of the dielectric functions ε and ε_{RPA} both approach constants. Equation (57) thus suggests that $f_{\text{xc}} \sim \chi_{\text{KS}}^{-1}$ can be used as the basis for constructing xc kernels which will have the correct long-range behavior, featuring density-dependent approximations of κ_{00} .

The first such approximation, termed the ‘‘bootstrap’’ kernel, was proposed by Sharma *et al.* [39, 84]:

$$f_{\text{xc}, \mathbf{G}\mathbf{G}'}^{\text{B}}(\mathbf{q}) = \frac{\varepsilon_{\mathbf{G}\mathbf{G}'}^{-1}(\mathbf{q}, \omega = 0)}{\chi_{00}^{\text{KS}}(\mathbf{q}, \omega = 0)}. \quad (58)$$

This approximate xc kernel can be related to the exact expression (57) by making three assumptions: (i) The head of the Kohn-Sham response function is dominant; (ii) in the denominator of Eq. (57), $\varepsilon - 1$ can be replaced by ε , which clearly works best for strong screening such as in small-gap semiconductors; (iii) ε and ε^{RPA} roughly differ by a constant (of order 1) in the \mathbf{q} -range of interest. These assumptions may hold under some circumstances, but are certainly not generally valid. Thus, Eq. (57) should best be viewed as a generalized LRC kernel with a somewhat more sophisticated form for the parameter α . In particular, the ‘‘bootstrapping’’ here means that the inverse dielectric function is constructed self-consistently using $f_{\text{xc}, \mathbf{G}\mathbf{G}'}^{\text{B}}(\mathbf{q})$ as input, i.e., $\varepsilon^{-1} = 1 + v\chi_s[1 - (v + f_{\text{xc}}^{\text{B}})\chi_s]^{-1}$.

To ensure that the bootstrap kernel is well defined, it should be implemented using the symmetrized quantities $f_{\text{xc}, \mathbf{G}\mathbf{G}'}^{\text{sym}}(\mathbf{q}) = v_{\mathbf{G}}^{-1/2}(\mathbf{q})f_{\text{xc}, \mathbf{G}\mathbf{G}'}(\mathbf{q})v_{\mathbf{G}'}^{-1/2}(\mathbf{q})$ and $\chi_{\mathbf{G}\mathbf{G}'}^{\text{sym}}(\mathbf{q}) =$

$v_{\mathbf{G}}^{1/2}(\mathbf{q})\chi_{\mathbf{G}\mathbf{G}'}(\mathbf{q})v_{\mathbf{G}'}^{1/2}(\mathbf{q})$. This then leads to the following form of the original bootstrap kernel [84]:

$$f_{\text{xc},\mathbf{G}\mathbf{G}'}^{\text{B}}(\mathbf{q}) = \frac{v_{\mathbf{G}}^{1/2}(\mathbf{q})\varepsilon_{\mathbf{G}\mathbf{G}'}^{-1}(\mathbf{q},0)v_{\mathbf{G}'}^{1/2}(\mathbf{q})}{1 - \varepsilon_{\text{RPA},00}(\mathbf{q},0)}, \quad (59)$$

where $v_{\mathbf{G}}(\mathbf{q}) = 4\pi/|\mathbf{q} + \mathbf{G}|^2$ is the Coulomb potential. In matrix form, the bootstrap kernel in the small- \mathbf{q} limit is given by

$$f_{\text{xc}}^{\text{B}} = \begin{pmatrix} \frac{\beta_{00}}{\mathbf{q}^2} & \frac{\beta_{01}}{|\mathbf{q}||\mathbf{G}_1|} & \frac{\beta_{02}}{|\mathbf{q}||\mathbf{G}_2|} & \cdots \\ \frac{\beta_{10}}{|\mathbf{G}_1||\mathbf{q}|} & \frac{\beta_{11}}{\mathbf{G}_1^2} & \frac{\beta_{12}}{|\mathbf{G}_1||\mathbf{G}_2|} & \cdots \\ \frac{\beta_{21}}{|\mathbf{G}_2||\mathbf{q}|} & \frac{\beta_{21}}{|\mathbf{G}_2||\mathbf{G}_1|} & \frac{\beta_{22}}{\mathbf{G}_2^2} & \cdots \\ \vdots & \vdots & \vdots & \ddots \end{pmatrix}, \quad (60)$$

where

$$\beta_{\mathbf{G}\mathbf{G}'} = \frac{4\pi\varepsilon_{\mathbf{G}\mathbf{G}'}^{-1}(\mathbf{q},0)}{1 - \varepsilon_{\text{RPA},00}(\mathbf{q},0)}. \quad (61)$$

If we compare the head element of f_{xc}^{B} to the head of the LRC kernel (49), we can define the LRC α -parameter for the Bootstrap kernel as

$$\alpha_{\text{B}} = \frac{4\pi\varepsilon_{00}^{-1}(0,0)}{\varepsilon_{\text{RPA},00}(0,0) - 1}. \quad (62)$$

We also consider two simpler variations of the Bootstrap kernel. The first one, referred to as the 0-Bootstrap kernel, is the Bootstrap kernel (60) without the built-in self-consistency. This means that $\varepsilon_{\mathbf{G}\mathbf{G}'}^{-1}(\mathbf{q},0)$ is replaced by $\varepsilon_{\text{RPA},\mathbf{G}\mathbf{G}'}^{-1}(\mathbf{q},0)$. The LRC α -parameter for the 0-Bootstrap kernel is thus given by

$$\alpha_{0\text{B}} = \frac{4\pi\varepsilon_{\text{RPA},00}^{-1}(0,0)}{\varepsilon_{\text{RPA},00}(0,0) - 1}. \quad (63)$$

The second simplified Bootstrap kernel is the RPA-Bootstrap kernel, first proposed by Rigamonti *et al.* [85]. This xc kernel is defined by replacing the self-consistent ε^{-1} with $\varepsilon_{\text{RPA}}^{-1}$, as in the 0-Bootstrap kernel above, and in addition by replacing the Kohn-Sham response function χ^{KS} in Eq. (58) with the RPA response function $\chi^{\text{RPA}} = \chi^{\text{KS}}/\varepsilon_{\text{RPA}}$. The associated head-only LRC α -parameter is

$$\alpha_{\text{RPAB}} = \frac{4\pi\varepsilon_{\text{RPA},00}^{-1}(0,0)}{1/\varepsilon_{\text{RPA},00}^{-1}(0,0) - 1}. \quad (64)$$

In a related development, Berger [86] combined the head-only RPA-Bootstrap kernel with the Vignale-Kohn functional of current-TDDFT [87–89]. The resulting formalism accounts for spectral line broadening from first principles, and also describes Drude tails in metallic systems.

4.5. The jellium-with-a-gap model

As we saw in Section 3.1, local and semilocal xc kernels (ALDA and GGAs) fail to give excitonic binding. From a physical standpoint this is hardly surprising: the construction of the ALDA and GGA xc kernels is based on the electron gas as reference system. An electron gas is a metallic system, that is, it does not have a gap. Therefore, (semi)local xc kernels are very good at describing plasmons, but simply do not contain the right physics to capture excitons.

It is natural to ask, then, whether one could find a reference system that does have a gap but is of a similar degree of simplicity as the electron gas. Such a system is known as the jellium-with-a-gap model (JGM), an idea that has been around for quite a while [90,91]. Based on the JGM model, Trevisanutto *et al.* proposed an xc kernel of the following limiting form [92]:

$$f_{\text{xc}}^{\text{JGM}}(q \rightarrow 0) = -\frac{E_g^2}{nq^2}, \quad (65)$$

where E_g is the energy gap of the JGM (in practice, the experimental gap), and n is taken as the local density. Expression (65) was derived by assuming that the head of the xc kernel goes as $f_{\text{xc}} \sim \chi_{\text{KS}}^{-1}$, see Eq. (57). The Kohn-Sham response function can then be expressed in terms of the RPA dielectric function, $\chi_{\text{KS}} = \frac{q^2}{4\pi}(1 - \varepsilon_{\text{RPA}})$, but Trevisanutto *et al.* replaced ε_{RPA} by the dielectric function of Levine and Louie [90], which has the limiting behavior $\varepsilon_{\text{JGM}}(q \rightarrow 0) = 1 + 4\pi n/E_g^2$. This immediately leads to Eq. (65).

The full form of the JGM xc kernel [92] (including \mathbf{G}, \mathbf{G}' -dependence) is constructed in such a way that it reduces to the static, \mathbf{q} -dependent xc kernel of the homogeneous electron gas of Ref. [93]. A simplified version of the JGM xc kernel was proposed by Patrick and Thygesen [94], and a gradient-corrected form was proposed by Terentjev *et al.* [95].

The JGM kernel is an empirical kernel since it requires the band gap as input, and its derivation relies on several ad-hoc assumptions. Owing to its $1/q^2$ long-range behavior, the JGM xc kernel belongs to the family of LRC kernels, where the parameter α depends on the local density (and, in the newest version [95], its gradients). As we will see, the performance of the JGM kernel is similar to that of the other kernels from the LRC family.

5. Practical considerations and assessment of xc kernels

5.1. Preliminary remarks: interfacing DFT and TDDFT

What is the proper way to assess approximate xc kernels of TDDFT? This is a rather complex question, and requires some discussion.

The formally correct way to do an approximate TDDFT calculation is as follows. First, find the self-consistent Kohn-Sham ground state with a given approximate xc potential $v_{\text{xc}}^{\text{gs,app}}(\mathbf{r})$, where the superscript “gs” indicates that it is an xc potential defined

within ground-state DFT. The approximate xc kernel f_{xc}^{app} to be investigated should be compatible with $v_{xc}^{\text{gs,app}}(\mathbf{r})$. This means that it is defined using Eq. (1) involving the functional derivative $\delta v_{xc}^{\text{app}}(\mathbf{r}, t)/\delta n(\mathbf{r}', t')$, where the time-dependent xc potential $v_{xc}^{\text{app}}(\mathbf{r}, t)$ reduces to $v_{xc}^{\text{gs,app}}(\mathbf{r})$ when it is evaluated at the stationary ground-state density $n_0(\mathbf{r})$. A typical example is the LDA ground state matched with an ALDA xc kernel.

This protocol has been followed in numerous studies, for instance in quantum chemistry, where TDDFT approximations were tested for molecular benchmark sets [96, 97]. In these studies, the same xc functionals were used to determine the Kohn-Sham ground states and to calculate the excitation energies. In other words, the xc kernels were always tested together with the underlying ground-state xc functionals.

The situation is very different when assessing TDDFT for excitonic effects in periodic solids. In essentially all studies, the approximations used for calculating the electronic band structure and for calculating the optical spectra with TDDFT are unrelated to each other. Most notably, the xc kernels belonging to the LRC family do not match the ground-state DFT approaches (such as LDA + scissors or *GW*) used for calculating the band structure. In fact, it turns out that many of the approximate xc kernels (such as the various forms of the bootstrap kernel) cannot even be written as functional derivatives at all!

This may be somewhat troubling from a formal perspective, but there are several points to keep in mind:

- Keeping the same method for the electronic band structure while testing different xc kernels allows one to assess the xc kernels just on their own merits.
- Using a band structure with the correct band gap as input to TDDFT will produce optical spectra in closer agreement with experiment. This makes the assessment of the excitonic xc kernels more systematic, and can tell us whether they produce the right answer for the right reasons. By contrast, an underestimated DFT band gap plus an underestimated TDDFT exciton binding energy can accidentally produce an excitonic peak just at the right position, simply by error cancellation.
- In Section 4.2.2 we showed that the xc kernel can be written as Eq. (43), and that the gap-opening effects of f_{xc}^{qp} can be approximated in various ways. Thus, one can always argue that approaches like the scissors operator are part of approximating the total xc kernel (the sum of quasiparticle plus excitonic contributions).

5.2. Choices of implementation

In the light of the above discussion, let us accept that we can test xc kernels independently of the method used for calculating the electronic band structure. To achieve a meaningful practical assessment of the xc kernels now requires making a number of choices and specifications, and to be clear and consistent with each of them. As indicated in Fig. 3, these choices can be grouped into three main categories: Band structure method, implementation of the xc kernel, and numerical details [98, 99].

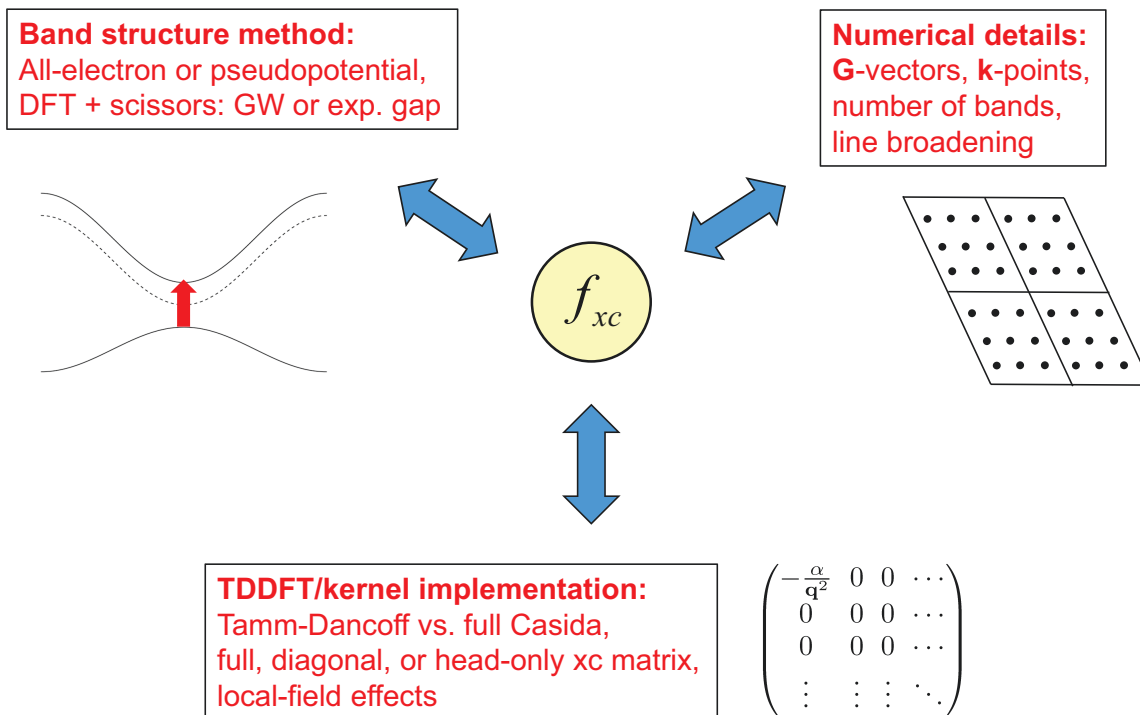


Figure 3. Schematic illustration of the many choices one needs to make when assessing the performance of excitonic xc kernels in TDDFT.

5.2.1. Band structure Each TDDFT calculation of optical spectra needs a ground-state electronic structure as input. Thus, the first choice to make is which code to use, and which methodology: all-electron or pseudopotential, and what type of basis (plane-wave, atom-centered, etc.). The differences between the outputs of the most popular codes are minor [100]. Here, we mainly worked with Abinit [30] and Quantum Espresso [101].

Once a code has been decided upon, the next choice concerns the method of calculation: DFT with semilocal functionals with or without scissors corrections [102,103], generalized DFT (hybrid functionals) [104–116], *GW* [2,20], or other methods. Standard local and semilocal xc functionals (LDA and GGAs), while computationally cheaper, tend to systematically underestimate band gaps, which means that the onset of absorption will be substantially redshifted. This can be easily corrected *ex post facto* by a simple rigid shift of the optical spectrum. We have often used this approach.

Hybrid functionals or *GW* produce band gaps E_g in much better, often excellent, agreement with experiment. However, differences remain: for instance, in wide-gap insulators the *GW* gap can be off by up to 1 eV. These differences can be comparable with the exciton binding energy E_b , which can lead to fortuitous error cancellations between errors in E_g and E_b .

The DFT+scissors approach is a computationally less costly, semiempirical approach to correct the band gap. The idea is that the conduction band energy levels $\varepsilon_{c\mathbf{k}}$ are shifted by an amount Δ with respect to the valence bands, i.e., $\varepsilon_{c\mathbf{k}} \rightarrow \varepsilon_{c\mathbf{k}} + \Delta$,

where Δ is the difference between the quasiparticle gap E_g and the Kohn-Sham gap. The former can be calculated from *GW* or taken from experiment. The scissors shift also implies that the momentum operator \hat{p} must be modified as follows [117]:

$$\hat{p} \rightarrow \left\{ \frac{\varepsilon_{c\mathbf{k}} + \Delta - \varepsilon_{v\mathbf{k}}}{\varepsilon_{c\mathbf{k}} - \varepsilon_{v\mathbf{k}}} \right\} \hat{p}. \quad (66)$$

In general, one would expect that the scissors operator simply causes a rigid shift of the entire optical spectrum, and does not have much impact on the calculation of excitonic effects. However, it turns out that excitonic effects using LRC kernels can be quite sensitive to the particular implementation of the scissors correction [99].

5.2.2. Implementation of the xc kernel In solving the BSE, it is standard practice to make the Tamm-Dancoff approximation (TDA), which significantly reduces the computational effort. It turns out that TDA is an excellent approximation for the BSE [61, 118], but not necessarily for TDDFT. We found [98] that the TDA significantly underestimates E_b of insulators using the bootstrap kernel, at times by more than a factor of two.

The next item to be decided is how to handle the so-called local-field effects, which come from the non-head elements (wings and body, with finite \mathbf{G}, \mathbf{G}') of the Hartree and xc kernels. Among other things, the local-field effects are responsible for the fact that $\epsilon_{00} \neq 1/\epsilon_{00}^{-1}$, which follows from calculating the dielectric tensor by solving the Dyson equation (11).

For all xc kernels of the matrix form (36) one has the choice of implementing the full matrix, the diagonal elements, or the head only. One typically finds [99] that the body of the LRC kernel has a relatively minor effect on the optical spectra of semiconductors, but can produce significantly different results for insulators [84, 85, 119, 120]. One therefore needs to state very clearly which version of the xc kernel is used: full, diagonal, or head-only.

5.2.3. Numerical details The accuracy of the excitonic effects predicted with TDDFT requires careful testing of convergence with respect to standard parameters: the number and geometric arrangement of \mathbf{k} -points, the number of \mathbf{G} -vectors, and the number of bands included in the construction of response functions, the Casida equation, or the bootstrap kernel. *GW*/BSE calculations of course require similar tests, but the convergence behavior can be quite different: we found that the BSE tends to need much fewer unoccupied conduction bands than TDDFT-LRC.

When calculating optical spectra, it is common practice to put in a Lorentzian line broadening by hand (alternatively, one can use frequency-dependent xc kernels [78, 86]). The Lorentzian line broadening simulates the effects of quasiparticle lifetimes, phonons, or disorder, with commonly used values in the range of 0.1 to 0.2 eV. The line broadening parameter obviously has a strong effect on spectral line shapes and peak heights; however, using it as a fitting tool to reproduce experimental spectral features should be avoided, especially if this involves broadening parameters outside the established range.

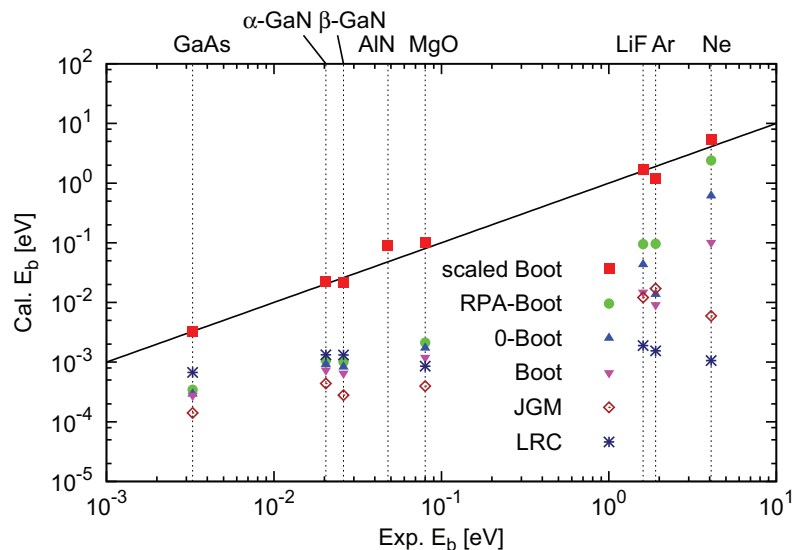


Figure 4. Comparison of experimental and calculated exciton binding energies E_b for various materials, using LRC-type xc kernels. The solid line indicates perfect agreement between theory and experiment. Reproduced with permission from [99] ©2017 American Physical Society.

5.2.4. Choice of materials Ideally, a good approximate xc functional in DFT or TDDFT should be universal, that is, it should work for any material. Thus, to assess the quality of excitonic xc kernels in an unbiased manner, it is important to test them for a range of different systems, including semiconductors, small-gap insulators, and wide-gap insulators. Ideally, the tested materials should include elemental solids, main-group binary compounds, oxides, as well as materials containing d -electrons. In addition, the xc kernels should also be tested for quasi two-dimensional systems. Needless to say, the computational cost of such systematic tests can be considerable.

5.3. Results

LRC-type kernels have been used in a number of applications to calculate optical properties of materials [121–129]. A critical assessment of LRC-type kernels was recently carried out [98,99] (for numerical details, please consult these references). In this section we will present an overview of the key results of this assessment, and give general recommendations for the use of LRC-type xc kernels in TDDFT.

5.3.1. Exciton binding energies and optical spectra Figure 4 shows exciton binding energies calculated for a range of materials, from semiconductors and small-gap insulators (GaAs, GaN) all the way to large-gap insulators (LiF, Ar, Ne). The calculations were done with the original LRC kernel (49)+(50), the jellium-with-a-gap model, and three versions of the bootstrap kernel (original, zero, and RPA). All of the above methods lead to a significant underestimation of the exciton binding energy

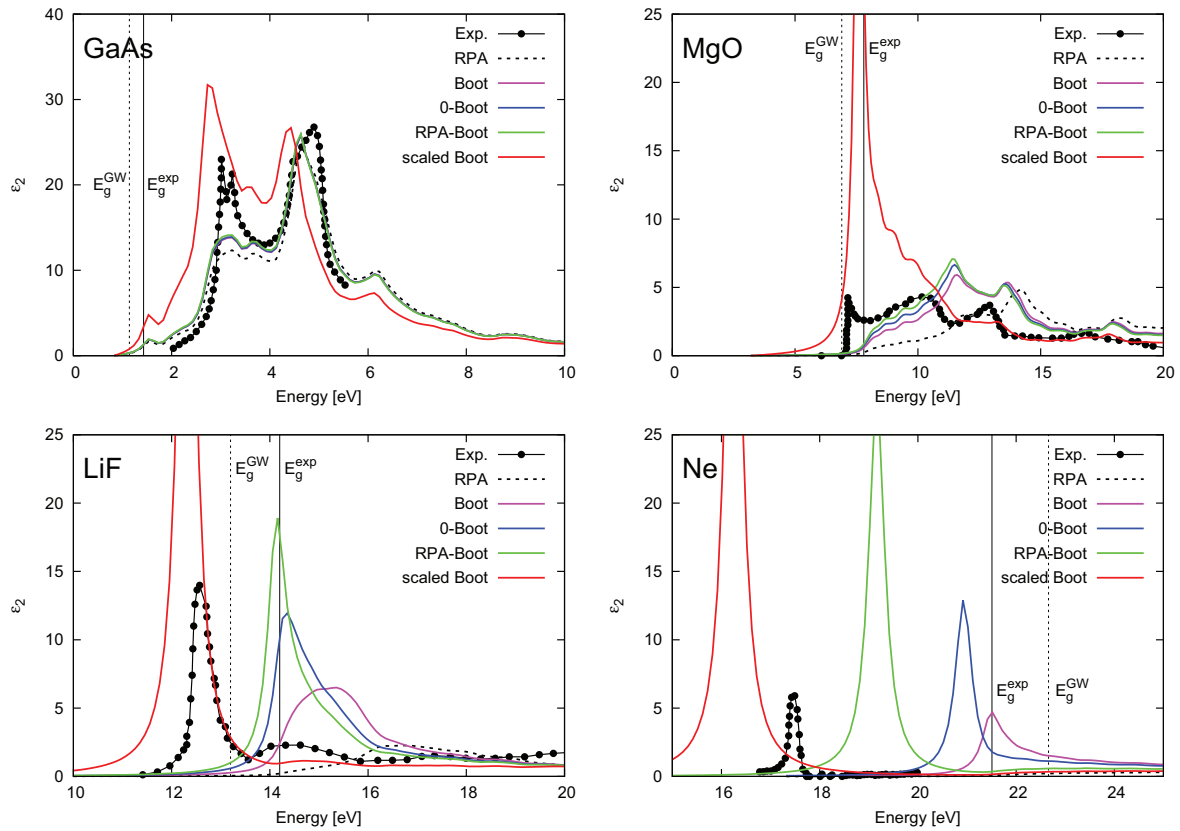


Figure 5. Calculated and experimental optical absorption spectra of GaAs, MgO, LiF, and Ne. Reproduced with permission from [99] ©2017 American Physical Society.

compared to experiment.

In addition to the kernels of the LRC family that were discussed in Section 4, an empirically scaled LRC kernel was introduced in Ref. [99], of the following form:

$$f_{xc}^{sB} = A(x) f_{xc}^{RPAB}, \quad (67)$$

where the material-dependent scaling factor $A(x)$ is a smooth function of $x = \epsilon_{RPA}^{-1}$, interpolating between $A \approx 1$ for large-gap insulators to $A \approx 6$ for semiconductors. The scaling factor $A(x)$ was empirically determined such that f_{xc}^{sB} produces exciton binding energy in agreement with experiment. Indeed, the red squares in Fig. 4 are very close to the experimental data.

The associated optical spectra for four of the materials, GaAs, MgO, LiF, and Ne, are shown in Fig. 5. The optical spectrum of GaAs has the well-known double-peak structure; the first peak at around 3 eV is a continuum exciton. The bound exciton is not visible on the scale of this plot. All LRC-type xc kernels underestimate the height of the continuum exciton peak, and the scaled bootstrap kernel somewhat overestimates it, but still reproduces the overall spectral shape.

The situation is very different for MgO. Here, the LRC-type kernels completely miss the bound exciton peak below the experimental gap. The f_{xc}^{sB} kernel, on the other

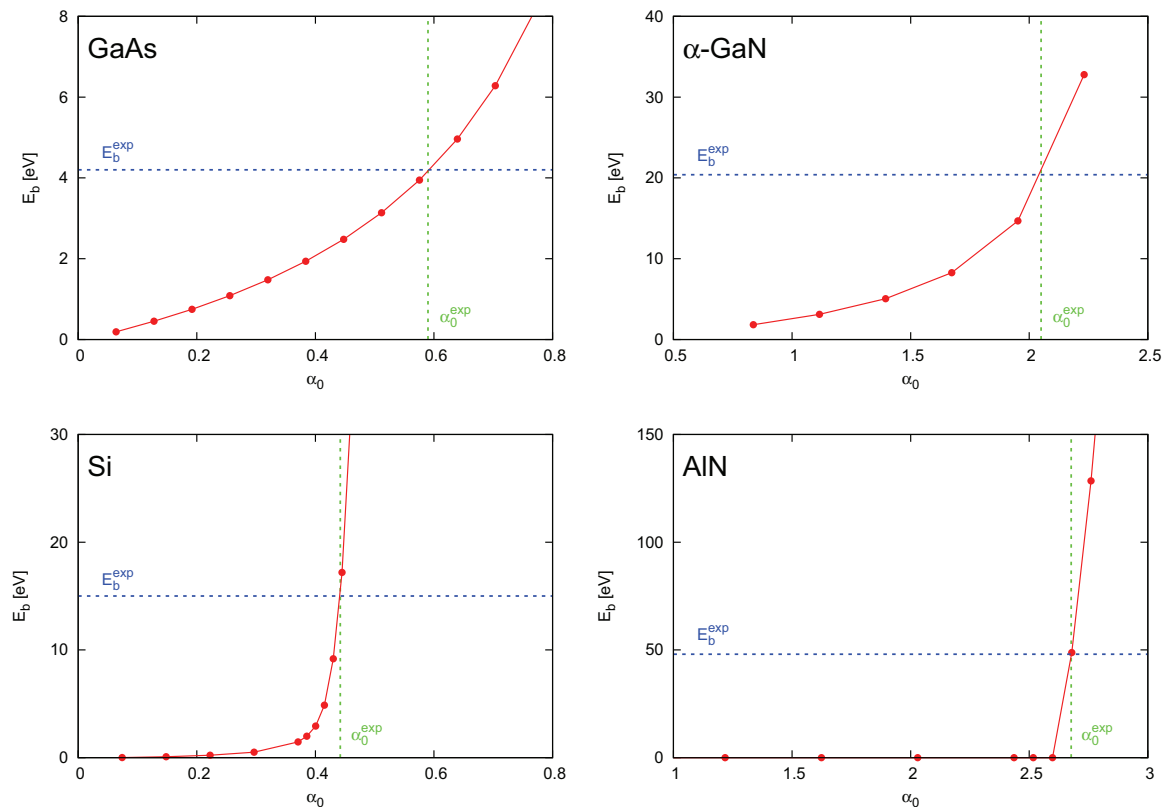


Figure 6. Exciton binding energy versus (head-only) LRC scaling parameter, illustrating the material-dependent sensitivity.

hand, creates a bound exciton peak at the right position, but completely distorts the spectral shape. Similar trends for MgO were observed in Ref. [95].

For the two cases with strongly bound excitons, LiF and solid Ne, we find again that the empirically scaled LRC kernel puts the exciton at the right position, but dramatically exaggerates the oscillator strength. In fact, looking at the case of Ne, we see that the increase of oscillator strength with E_b closely follows the $\sqrt{E_b}$ behavior that was predicted from the Wannier model in Section 2, see Fig. 1b.

From these results, we conclude that with static LRC-type xc kernels it is impossible to obtain correct exciton binding energies and good spectral shapes at the same time. If we choose approximations that deliver good E_b , the oscillator strengths tend to be drastically exaggerated. In fact, this suggests that the xc kernel must have a pronounced frequency-dependence behavior, even for weakly bound excitons such as in silicon [46].

5.3.2. Sensitivity of the LRC-type kernels Getting the correct exciton binding energy of a material is still a significant accomplishment for TDDFT, even if the peak height is wrong. The scaled bootstrap kernel (67), or any other empirically scaled LRC-type kernel, could therefore be quite useful in practice. However, for some materials, scaled LRC kernels are plagued by an extremely high sensitivity.

Table 1. Evaluation of Eq. (68) for the materials shown in Fig. 6.

	$ \chi_{00}^{\text{KS}} /q^2$	E_g (eV)	E_b (meV)	$dE_b/d\alpha$
GaAs	11.18	0.86	4.2	45
α -GaN	5.50	1.97	20	110
Si	13.98	0.59	15.2	210
AlN	5.14	4.34	46	236

In Fig. 6 we plot E_b versus the LRC parameter α , see Eq. (49), for GaAs, α -GaN, Si and AlN. In all materials, E_b increases with α , but the rate of increase is vastly different. Whereas the slope $dE_b/d\alpha$ is moderate around the experimental value for GaAs and α -GaN, the slope is extremely steep for Si and AlN. In other words, small fluctuations of the LRC parameter cause huge differences of the exciton binding energy. This sensitivity makes it extremely hard to come up with a universal, useful model xc kernel based on LRC.

It is possible to approximately predict the sensitivity of the LRC kernel for a given material. We show in Appendix B that

$$\frac{dE_b}{d\alpha} \approx \lim_{\mathbf{q} \rightarrow 0} \frac{E_b}{q^2} \chi_{00}^{\text{KS}}(\mathbf{q}, \omega). \quad (68)$$

Thus, the sensitivity of the LRC kernel is determined by the electronic band structure via the head of the Kohn-Sham response function. In Table 1 we evaluate Eq. (68) for the materials shown in Fig. 6, using the experimental values of E_b as input. The rightmost column shows that our estimates produce the right ordering of the materials according to their sensitivity.

5.3.3. How should LRC xc kernels be used? All tests and assessments of the various types of LRC kernels have shown that they cannot reproduce all aspects of excitonic optical spectra, but only certain parts. Typically, the xc kernels proposed in the literature, such as bootstrap or jellium-with-a-gap, underestimate the exciton binding energy, but yield decent peak heights of bound excitons or continuum excitons. This suggests that there are two ways in which LRC kernels can be properly used.

The first approach takes advantage of the fact that LRC kernels can produce good line shapes, but put the bound excitons at the wrong position. Thus, in addition to the LRC parameter α one can introduce an empirical correction into the scissors shift. This is illustrated in Fig. 7, which shows results for lithium niobate LiNbO_3 [125]. The original bootstrap and RPA bootstrap kernels produce a wrong exciton peak height, compared to the BSE (dashed red line). The best results (black line) are achieved using the simple LRC kernel (49) with a value of $\alpha = 0.44$ and a scissors shift that is reduced from 2 eV to 1.4 eV.

The second approach is the semi-quantitative calculation of exciton binding energies E_b using an empirical scaling model [99]. As we have seen, this method only works reliably for materials where the LRC-type kernels are not very sensitive to fluctuations

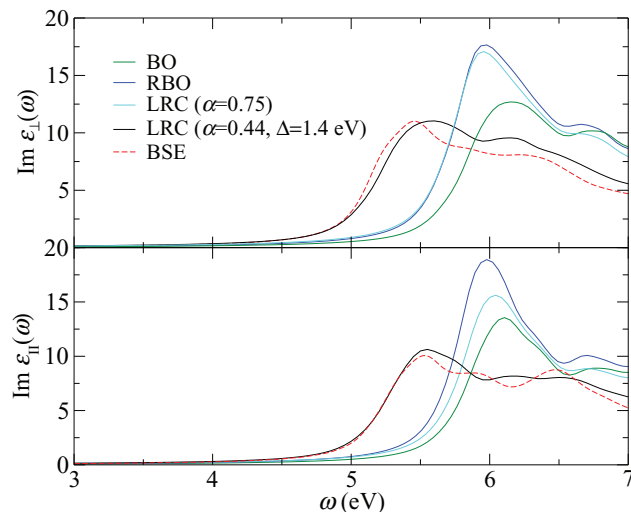


Figure 7. Optical spectra of lithium niobate, comparing several approximate xc kernels with BSE. Here, BO stands for bootstrap, RPA stands for RPA bootstrap, and LRC stands for the xc kernel (49). Reproduced with permission from [125] ©2017 American Physical Society.

of the scaling parameter. An example where this approach could be very useful is for calculating excitonic effects in semiconductor alloys, or in materials with defects.

6. Generalized TDDFT: hybrid kernels for excitons

We now briefly discuss an alternative approach to the calculation of optical properties in solids, based on generalized TDDFT using hybrid functionals. Over the past decade, there have been several applications of hybrid xc functionals to describe excitations in periodic solids [130–133]. In particular, the so-called optimally tuned range-separated hybrids have been shown to yield good results for organic molecular crystals [26, 134], see the right panel of Fig. 8. More recently, range-separated hybrids with an empirical parameter were shown to agree well with GW/BSE results for several materials [135, 136].

There is a direct connection between the BSE and generalized TDDFT [137, 138]. The BSE can be expressed as a matrix equation similar in form to the Casida equation of TDDFT, Eqs. (16), (17). Making the Tamm-Dancoff approximation, one obtains

$$[(\varepsilon_{c\mathbf{k}} - \varepsilon_{v\mathbf{k}'})\delta_{vv'}\delta_{cc'}\delta_{\mathbf{k}\mathbf{k}'} + K_{cv\mathbf{k},c'v'\mathbf{k}'}^{\text{BSE}}] \mathbf{Y} = \omega \mathbf{Y}. \quad (69)$$

Here, v and c denote occupied valence and unoccupied conduction bands, respectively. Equation (69) features the BSE coupling matrix $K^{\text{BSE}} = K^{\text{d}} + K^{\text{x}}$. The first part of K^{BSE} is the direct (Hartree) interaction,

$$K^{\text{d}} = \frac{2}{\mathcal{V}} \sum_{\mathbf{G} \neq 0} \frac{4\pi}{|\mathbf{G}|^2} \langle c\mathbf{k} | e^{i\mathbf{G}\cdot\mathbf{r}} | v\mathbf{k} \rangle \langle v'\mathbf{k}' | e^{-i\mathbf{G}\cdot\mathbf{r}} | c'\mathbf{k}' \rangle. \quad (70)$$

The second part is the exchange kernel,

$$K^x = \frac{2}{\mathcal{V}} \sum_{\mathbf{G}\mathbf{G}'} W_{\mathbf{G}\mathbf{G}'}(\mathbf{q}, \omega) \delta_{\mathbf{q}, \mathbf{k}-\mathbf{k}'} \langle c\mathbf{k} | e^{i(\mathbf{q}+\mathbf{G})\cdot\mathbf{r}} | c'\mathbf{k}' \rangle \langle v'\mathbf{k}' | e^{-i(\mathbf{q}+\mathbf{G}')\cdot\mathbf{r}} | v\mathbf{k} \rangle, \quad (71)$$

which contains the screened Coulomb interaction

$$W_{\mathbf{G}\mathbf{G}'}(\mathbf{q}, \omega) = -\frac{4\pi\epsilon_{\mathbf{G}\mathbf{G}'}^{-1}(\mathbf{q}, \omega)}{|\mathbf{q} + \mathbf{G}||\mathbf{q} + \mathbf{G}'|}, \quad (72)$$

featuring the RPA inverse dielectric function $\epsilon_{\mathbf{G}\mathbf{G}'}^{-1}(\mathbf{q}, \omega)$. In most applications of the BSE, one uses the static limit $\epsilon_{\mathbf{G}\mathbf{G}'}^{-1}(\mathbf{q}, \omega = 0)$. But even then, the RPA calculation for the dielectric function remains a computational bottleneck, requiring a summation over the \mathbf{q} -grid in addition to a double sum over $\mathbf{G}\mathbf{G}'$. Furthermore, a fully converged ϵ^{-1} usually requires including many unoccupied bands.

If one were to ignore dielectric screening by setting $\epsilon^{-1} = 1$ in Eq. (72), one would arrive at the time-dependent Hartree-Fock (TDHF) approach. It is well known that this leads to a drastic overbinding of excitons (except in extreme cases of strongly bound excitons such as in solid Ar or Ne), which can cause a complete spectral collapse.

A simple compromise between the BSE (full dielectric screening) and TDHF (no screening) is to use a simplified form of dielectric screening. Yang *et al.* [137] proposed to replace the dielectric matrix with a single screening parameter γ , diagonal in $\mathbf{G}\mathbf{G}'$:

$$\epsilon_{\mathbf{G}\mathbf{G}'}^{-1}(\mathbf{q}, \omega = 0) \rightarrow \gamma \delta_{\mathbf{G}\mathbf{G}'}. \quad (73)$$

The screening parameter can be calculated from first principles as $\gamma = (\epsilon^{\text{RPA}})_{00}^{-1}(\mathbf{q} = 0)$. Alternately, one can use a more sophisticated model,

$$\epsilon_{\mathbf{G}\mathbf{G}'}^{-1}(\mathbf{q}, \omega = 0) \rightarrow \epsilon_m(q)^{-1} \delta_{\mathbf{G}\mathbf{G}'}, \quad (74)$$

where $\epsilon_m(q)$ is a model dielectric function [139]. Recently, Sun *et al.* [138] performed an assessment of these two approximations, (73) and (74), termed screened exact exchange (SXX) and model-BSE (m-BSE), respectively. In addition, a simple nonempirical hybrid xc kernel for generalized TDDFT was proposed [138]:

$$K_{\text{xc}}^{\text{hybrid}} = K^{\text{SXX}} + (1 - \gamma)K_{\text{xc}}^{\text{ALDA}}. \quad (75)$$

It was found that all three approximations, SXX, m-BSE and the hybrid kernel (75), produce exciton binding energies in closed agreement with the BSE, at a much reduced computational cost. An illustration for LiF is shown in Fig. 8, left panel. Not only is the excitonic peak at the right position, it also has the right oscillator strength.

Thus, generalized TDDFT using specialized hybrid kernels is beginning to emerge as a very promising and cost-effective alternative to full BSE calculations. However, compared to pure TDDFT, especially if using simple LRC-type xc kernels, the computational effort of these hybrid approaches is still significantly higher.

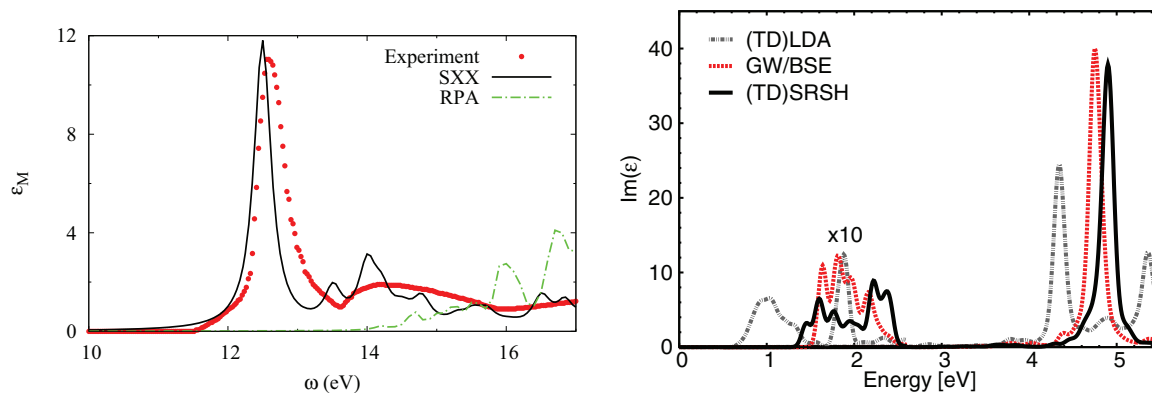


Figure 8. Left: optical spectrum of LiF, comparing experimental data with RPA and with the SXX approach, Eq. (73). Reproduced with permission from [137] ©2015 American Physical Society. Right: optical spectrum of crystalline pentacene, comparing BSE with ALDA and the optimally tuned range-separated hybrid approach. Reproduced with permission from [134] ©2015 American Physical Society.

7. Conclusions and outlook

In this paper we have reviewed the TDDFT linear-response formalism for first-principles calculations of optical spectra in periodic solids. The approach, while in principle exact, heavily relies on finding suitable approximate xc kernels. The standard semilocal approximations (LDA and GGAs) that have been so successful in many areas of science do not work for excitons; this has motivated the development of new approaches specific to the description of periodic semiconductors and insulators.

The development of excitonic xc kernels for TDDFT, which began with the groundbreaking work of Reining *et al.* in 2002 [2, 42], has led to a number of approximations of various degrees of sophistication. The common feature of all successful excitonic xc kernels is their $1/q^2$ long-range behavior. In fact, the $1/q^2$ -feature alone is already sufficient to construct a rudimentary xc kernel, known as the long-range corrected (LRC) kernel, which successfully reproduces parts of the optical spectrum in insulators and semiconductors. This was recognized early on [42, 49], and over the years has formed the basis for the development of a number of other xc kernels, such as the bootstrap kernel or the jellium-with-a-gap model, which we have here referred to as the family of LRC-type kernels.

A detailed numerical assessment of the family of LRC-type xc kernels has shown their potential as well as their limitations. On the plus side, LRC kernels are numerically very simple and efficient, especially compared to full *GW*/*BSE* calculations. With some tricks (such as empirically adjusting the strength of the head of the xc kernel, and introducing a variable scissors shift), LRC kernels can produce useful results for parts of the optical spectrum. In particular, they can be used to obtain semiquantitative results for systems that are too complex to be treated with full BSE.

On the other hand, it is now clear that there are no LRC-type kernels which

universally work for all materials, and for all aspects of the optical spectra in semiconductors and insulators. With the presently used xc kernels, it is impossible to obtain accurate exciton binding energies and spectral oscillator strengths at the same time. Furthermore, applications are often plagued by strong sensitivity with regard to the numerical implementation and the material under consideration. This means that empirically fitted parametrizations strongly depend on the choices of numerical implementation, and will have to be refit for other choices.

There are several directions to move the field forward. First of all, better xc kernels for the optical properties of periodic solids are needed. The current generation of LRC-type xc kernels, notably the bootstrap kernels, suffer from the lack of a convincing derivation. Furthermore, the practical implementation is often limited to head-only or diagonal in $\mathbf{G}\mathbf{G}'$. To remedy the deficiencies mentioned above, it will be crucial to take advantage of the full, nonlocal matrix form of the xc kernel. This will require new derivations, with guidance from many-body physics.

As we discussed, hybrid functionals may be a promising alternative, although at a somewhat elevated computational cost. One of the main advantages of hybrid functionals is that in this way one can match ground-state DFT (with good band gaps) and TDDFT (with good optical spectra), using the same type functional, rather than two unrelated approaches.

Lastly, there has been increased activity in real-time TDDFT for periodic solids in the past few years [65, 140–147]. A real-time TDDFT description of excitonic effects in semiconductors and insulators would be of tremendous interest for many applications in optoelectronics and ultrafast spectroscopy. This will require a proper account of long-range xc effects, along similar lines as in the linear-response TDDFT framework discussed here.

Acknowledgments

This work was supported by NSF grant No. DMR-1810922. The computation for this work was performed on the high performance computing infrastructure provided by Research Computing Support Services at the University of Missouri-Columbia.

Appendix A. Derivation of the Casida equation

Starting point of the derivation of the Casida equation for periodic solids is the response equation (15) without external perturbing potential:

$$n_{1\mathbf{G}}(\mathbf{k}, \omega) = \sum_{\mathbf{G}'} \chi_{\mathbf{G}\mathbf{G}'}^{\text{KS}}(\mathbf{k}, \omega) \sum_{\mathbf{G}''} f_{\mathbf{G}'\mathbf{G}''}^{\text{Hxc}}(\mathbf{k}, \omega) n_{1\mathbf{G}''}(\mathbf{k}, \omega). \quad (\text{A.1})$$

We multiply both sides from the left with the Hxc kernel, and sum over \mathbf{G} . Defining $g_{\mathbf{G}_1} = \sum_{\mathbf{G}} f_{\mathbf{G}_1\mathbf{G}}^{\text{Hxc}} n_{1\mathbf{G}}$ and using the explicit expression (13) of the Kohn-Sham response

function, this leads to

$$g_{\mathbf{G}_1}(\mathbf{k}, \omega) = \frac{2}{\mathcal{V}} \sum_{\mathbf{k}'jl} \frac{f_{j\mathbf{k}'} - f_{l\mathbf{k}+\mathbf{k}'}}{\omega - \varepsilon_{l\mathbf{k}+\mathbf{k}'} + \varepsilon_{j\mathbf{k}'} + i\eta} \sum_{\mathbf{G}} f_{\mathbf{G}_1\mathbf{G}}^{\text{Hxc}}(\mathbf{k}, \omega) \\ \times \langle j\mathbf{k}' | e^{-i(\mathbf{k}+\mathbf{G})\cdot\mathbf{r}} | l\mathbf{k} + \mathbf{k}' \rangle \sum_{\mathbf{G}'} \langle l\mathbf{k} + \mathbf{k}' | e^{i(\mathbf{k}+\mathbf{G}')\cdot\mathbf{r}} | j\mathbf{k}' \rangle g_{\mathbf{G}'}(\mathbf{k}, \omega). \quad (\text{A.2})$$

Introducing $H_{l'j'\mathbf{k}''}(\mathbf{k}, \omega) = \sum_{\mathbf{G}_1} \langle l'\mathbf{k} + \mathbf{k}'' | e^{i(\mathbf{k}+\mathbf{G}_1)\cdot\mathbf{r}} | j'\mathbf{k}'' \rangle g_{\mathbf{G}_1}(\mathbf{k}, \omega)$, we obtain

$$H_{l'j'\mathbf{k}''}(\mathbf{k}, \omega) = \sum_{\mathbf{k}'jl} \frac{f_{j\mathbf{k}'} - f_{l\mathbf{k}+\mathbf{k}'}}{\omega - \varepsilon_{l\mathbf{k}+\mathbf{k}'} + \varepsilon_{j\mathbf{k}'} + i\eta} K_{l'j'\mathbf{k}'',lj\mathbf{k}'}(\mathbf{k}, \omega) H_{lj\mathbf{k}'}(\mathbf{k}, \omega), \quad (\text{A.3})$$

where we define the coupling matrix elements

$$K_{l'j'\mathbf{k}'',lj\mathbf{k}'}(\mathbf{k}, \omega) = \frac{2}{\mathcal{V}} \sum_{\mathbf{G}\mathbf{G}_1} \langle l'\mathbf{k} + \mathbf{k}'' | e^{i(\mathbf{k}+\mathbf{G}_1)\cdot\mathbf{r}} | j'\mathbf{k}'' \rangle f_{\mathbf{G}_1\mathbf{G}}^{\text{Hxc}}(\mathbf{k}, \omega) \\ \times \langle j\mathbf{k}' | e^{-i(\mathbf{k}+\mathbf{G})\cdot\mathbf{r}} | l\mathbf{k} + \mathbf{k}' \rangle. \quad (\text{A.4})$$

Next, we drop the infinitesimal $i\eta$ in the denominator, which can be justified assuming a discretized \mathbf{k} -space, and define

$$\beta_{lj\mathbf{k}'}(\mathbf{k}, \omega) = \frac{H_{lj\mathbf{k}'}(\mathbf{k}, \omega)}{\omega - \varepsilon_{l\mathbf{k}+\mathbf{k}'} + \varepsilon_{j\mathbf{k}'}}. \quad (\text{A.5})$$

Equation (A.3) then becomes

$$\sum_{\mathbf{k}'jl} \left[(\varepsilon_{l'\mathbf{k}+\mathbf{k}''} - \varepsilon_{j'\mathbf{k}''}) \delta_{jj'} \delta_{ll'} \delta_{\mathbf{k}'\mathbf{k}''} \right. \\ \left. + (f_{j\mathbf{k}'} - f_{l\mathbf{k}+\mathbf{k}'}) K_{l'j'\mathbf{k}'',lj\mathbf{k}'}(\mathbf{k}, \omega) \right] \beta_{lj\mathbf{k}'}(\mathbf{k}, \omega) = \omega \beta_{l'j'\mathbf{k}''}(\mathbf{k}, \omega). \quad (\text{A.6})$$

Now let us specifically consider optical excitations with $\mathbf{k} = 0$. With this, Eq. (A.6) simplifies to

$$\sum_{\mathbf{k}'jl} [(\varepsilon_{l'\mathbf{k}} - \varepsilon_{j'\mathbf{k}}) \delta_{jj'} \delta_{ll'} \delta_{\mathbf{k}\mathbf{k}'} + (f_{j\mathbf{k}'} - f_{l\mathbf{k}'}) K_{l'j'\mathbf{k}',lj\mathbf{k}'}] \beta_{lj\mathbf{k}'} = \omega \beta_{l'j'\mathbf{k}}. \quad (\text{A.7})$$

Only transitions between occupied and empty bands will contribute, and the occupation numbers are simply 0 or 1. We can then rewrite (A.7) as two equations:

$$\sum_{\mathbf{k}'jb} [(\varepsilon_{i\mathbf{k}} - \varepsilon_{a\mathbf{k}}) \delta_{ji} \delta_{ba} \delta_{\mathbf{k}\mathbf{k}'} \beta_{jb\mathbf{k}'} - K_{ia\mathbf{k},jb\mathbf{k}'} \beta_{jb\mathbf{k}'} + K_{ia\mathbf{k},bj\mathbf{k}'} \beta_{bj\mathbf{k}'}] = \omega \beta_{ia\mathbf{k}} \quad (\text{A.8})$$

$$\sum_{\mathbf{k}'jb} [(\varepsilon_{a\mathbf{k}} - \varepsilon_{i\mathbf{k}}) \delta_{ba} \delta_{ji} \delta_{\mathbf{k}\mathbf{k}'} \beta_{bj\mathbf{k}'} - K_{ai\mathbf{k},jb\mathbf{k}'} \beta_{jb\mathbf{k}'} + K_{ai\mathbf{k},bj\mathbf{k}'} \beta_{bj\mathbf{k}'}] = \omega \beta_{ai\mathbf{k}} \quad (\text{A.9})$$

where a, b are indices of empty bands and i, j are indices of occupied bands. Lastly, defining $X_{ia\mathbf{k}} = -\beta_{ia\mathbf{k}}$ and $Y_{ia\mathbf{k}} = \beta_{ai\mathbf{k}}$ we end up with Eqs. (16) and (17). These two coupled equations can be represented as a single equation of the matrix-vector form

$$\begin{pmatrix} \mathbf{A} & \mathbf{B} \\ \mathbf{B}^* & \mathbf{A}^* \end{pmatrix} \begin{pmatrix} \mathbf{X} \\ \mathbf{Y} \end{pmatrix} = \omega \begin{pmatrix} -1 & 0 \\ 0 & 1 \end{pmatrix} \begin{pmatrix} \mathbf{X} \\ \mathbf{Y} \end{pmatrix}, \quad (\text{A.10})$$

and this is what is usually referred to as the Casida equation [10, 37].

Appendix B. Derivation of Eq.(68)

In this Appendix we provide details of the derivation of Eq. (68).

Starting point is the Casida equation for periodic solids, Eqs. (16) and (17). Within the Tamm-Dancoff approximation, and using a two-band model with only one valence band v and one conduction band c , the Casida equation reduces to

$$\sum_{\mathbf{k}'} [(\varepsilon_{c\mathbf{k}} - \varepsilon_{v\mathbf{k}})\delta_{\mathbf{k}\mathbf{k}'} + K_{cv\mathbf{k},cv\mathbf{k}'}] Y_{v\mathbf{k}\mathbf{k}'} = \omega Y_{v\mathbf{k}\mathbf{k}}. \quad (\text{B.1})$$

The eigenvectors $Y_{v\mathbf{k}\mathbf{k}}$ reflect the mixing of \mathbf{k} -states in an excitation. For instance, for single-particle excitations in the continuum, $Y_{v\mathbf{k}\mathbf{k}}$ is peaked at a single \mathbf{k} -value, whereas for bound excitons a whole range of \mathbf{k} -values contributes. We will now make the rather drastic approximation that the exciton mixes all k -states equally, setting $Y_{v\mathbf{k}\mathbf{k}} \sim \text{const.}$ This is certainly true for the states close to the band gap, which are dominant in the formation of the exciton. The constant follows from the normalization condition $1 = \sum_{\mathbf{k}} Y_{v\mathbf{k}\mathbf{k}}^* Y_{v\mathbf{k}\mathbf{k}}$ so that $Y_{v\mathbf{k}\mathbf{k}} = 1/\sqrt{V_{\text{BZ}}}$, where V_{BZ} is the volume of the first BZ.

Next, let us consider the coupling matrix $K_{cv\mathbf{k},cv\mathbf{k}'}$. Using a head-only xc kernel and dropping the Hartree part, the coupling matrix becomes

$$K_{v\mathbf{k}\mathbf{k},v'\mathbf{k}'\mathbf{k}'} = \lim_{\mathbf{q} \rightarrow 0} \frac{2}{\mathcal{V}} \langle v\mathbf{k} | e^{i\mathbf{q}\cdot\mathbf{r}} | c\mathbf{k} \rangle f_{00}^{\text{xc}}(\mathbf{q}) \langle c'\mathbf{k}' | e^{-i\mathbf{q}\cdot\mathbf{r}} | v'\mathbf{k}' \rangle, \quad (\text{B.2})$$

where we consider α -dependent LRC kernels $f_{00}^{\text{xc}}(\mathbf{q}) = -\alpha/q^2$. Substituting this into Eq. (B.1), and taking the derivative with respect to α on both sides, leads to

$$-\lim_{\mathbf{q} \rightarrow 0} \frac{2}{\mathcal{V}} \frac{1}{V_{\text{BZ}}} \sum_{\mathbf{k}\mathbf{k}'} \langle v\mathbf{k} | e^{i\mathbf{q}\cdot\mathbf{r}} | c\mathbf{k} \rangle \frac{1}{q^2} \langle c\mathbf{k}' | e^{-i\mathbf{q}\cdot\mathbf{r}} | v\mathbf{k}' \rangle = \frac{d\omega}{d\alpha}. \quad (\text{B.3})$$

Next, we consider the Kohn-Sham response function, Eq. (13). The head of the response function, in the two-band model and in the limit $\mathbf{q} \rightarrow 0$, is

$$\begin{aligned} \chi_{00}^{\text{KS}}(\mathbf{q} \rightarrow 0, \omega) &= \frac{2}{\mathcal{V}} \sum_{\mathbf{k}} \frac{1}{\omega + \varepsilon_{v\mathbf{k}} - \varepsilon_{c\mathbf{k}}} \langle v\mathbf{k} | e^{-i\mathbf{q}\cdot\mathbf{r}} | c\mathbf{k} \rangle \langle c\mathbf{k} | e^{i\mathbf{q}\cdot\mathbf{r}'} | v\mathbf{k} \rangle \\ &\quad - \frac{2}{\mathcal{V}} \sum_{\mathbf{k}} \frac{1}{\omega + \varepsilon_{c\mathbf{k}} - \varepsilon_{v\mathbf{k}}} \langle c\mathbf{k} | e^{-i\mathbf{q}\cdot\mathbf{r}} | v\mathbf{k} \rangle \langle v\mathbf{k} | e^{i\mathbf{q}\cdot\mathbf{r}'} | c\mathbf{k} \rangle. \end{aligned} \quad (\text{B.4})$$

We keep only the dominant (resonant) terms and drop the antiresonant ones, and we approximate the difference of the single-particle energies by $\varepsilon_{c\mathbf{k}} - \varepsilon_{v\mathbf{k}} \approx E_g$. Since the exciton binding energy is $E_b = E_g - \omega$, the response function becomes

$$\chi_{00}^{\text{KS}}(\mathbf{q} \rightarrow 0, \omega) = -\frac{2}{\mathcal{V}} \frac{1}{E_b} \sum_{\mathbf{k}} |\langle v\mathbf{k} | e^{i\mathbf{q}\cdot\mathbf{r}} | c\mathbf{k} \rangle|^2. \quad (\text{B.5})$$

Eqs. (B.3) and (B.5) are very similar, except that in Eq. (B.3) there is an extra summation over \mathbf{k}' . However, one may get rid of it by arguing that the Bloch states $|c\mathbf{k}\rangle$ and $|v\mathbf{k}\rangle$ are plane-wave-like (which, by the way, is one of the key assumption of the Wannier model). Equation (B.3) can thus be written as

$$-\lim_{\mathbf{q} \rightarrow 0} \frac{2}{\mathcal{V}} \frac{1}{q^2} \sum_{\mathbf{k}} |\langle v\mathbf{k} | e^{i\mathbf{q}\cdot\mathbf{r}} | c\mathbf{k} \rangle|^2 = \frac{d\omega}{d\alpha}. \quad (\text{B.6})$$

Comparison with Eq. (B.5) then gives the desired final result:

$$\frac{d\omega}{d\alpha} = \lim_{\mathbf{q} \rightarrow 0} \frac{E_b}{q^2} \chi_{00}^{\text{KS}}(\mathbf{q}, \omega). \quad (\text{B.7})$$

- [1] P. Yu and M. Cardona. *Fundamentals of Semiconductors*. Springer, Berlin, 4th edition, 2010.
- [2] G. Onida, L. Reining, and A. Rubio. Electronic excitations: density-functional versus many-body Green's-function approaches. *Rev. Mod. Phys.*, 74:601, 2002.
- [3] G. Stefanucci and R. van Leeuwen. *Nonequilibrium many-body theory of quantum systems*. Cambridge University Press, Cambridge, 2013.
- [4] F. Bechstedt. *Many-body approach to electronic excitations*. Springer, Berlin, 2015.
- [5] R. M. Martin, L. Reining, and D. M. Ceperley. *Interacting Electrons: Theory and Computational Approaches*. Cambridge University Press, Cambridge, 2016.
- [6] P. Hohenberg and W. Kohn. Inhomogeneous electron gas. *Phys. Rev.*, 136:B864–71, 1964.
- [7] W. Kohn and L. J. Sham. Self-consistent equations including exchange and correlation effects. *Phys. Rev.*, 140:A1133–8, 1965.
- [8] W. Kohn. Nobel lecture: electronic structure of matter—wave functions and density functionals. *Rev. Mod. Phys.*, 71:1253–66, 1999.
- [9] E. Runge and E. K. U. Gross. Density-functional theory for time-dependent systems. *Phys. Rev. Lett.*, 52:997–1000, 1984.
- [10] C. A. Ullrich. *Time-dependent density-functional theory: concepts and applications*. Oxford University Press, Oxford, 2012.
- [11] N. T. Maitra. Perspective: Fundamental aspects of time-dependent density functional theory. *J. Chem. Phys.*, 144:220901–1–16, 2016.
- [12] L. J. Sham and T. M. Rice. Many-particle derivation of the effective-mass equation for the Wannier exciton. *Phys. Rev.*, 144:708–14, 1966.
- [13] W. Hanke and L. J. Sham. Many-particle effects in the optical excitations of a semiconductor. *Phys. Rev. Lett.*, 43:387–90, 1979.
- [14] W. Hanke and L. J. Sham. Many-particle effects in the optical spectrum of a semiconductor. *Phys. Rev. B*, 21:4656–73, 1980.
- [15] G. Strinati. Application of the Green's functions method to the study of the optical properties of semiconductors. *Riv. Nuovo Cimento*, 11:1–86, 1988.
- [16] L. X. Benedict, E. L. Shirley, and R. B. Bohn. Optical absorption of insulators and the electron-hole interaction: An ab initio calculation. *Phys. Rev. Lett.*, 80:4514–7, 1998.
- [17] M. Rohlfing and S. G. Louie. Electron-hole excitations in semiconductors and insulators. *Phys. Rev. Lett.*, 81:2312–5, 1998.
- [18] M. Rohlfing and S. G. Louie. Electron-hole excitations and optical spectra from first principles. *Phys. Rev. B*, 62:4927, 2000.
- [19] L. Hedin. New method for calculating the one-particle Green's function with application to the electron-gas problem. *Phys. Rev.*, 139:A796–A823, 1965.
- [20] F. Aryasetiawan and O. Gunnarsson. The GW method. *Rep. Prog. Phys.*, 61:237–312, 1998.
- [21] S. Ismail-Beigi. First principles calculation of optical and electronic properties with inclusion of exciton effects. *Phys. Stat. Sol. (c)*, 3:3365–72, 2006.
- [22] P. Puschnig and C. Ambrosch-Draxl. Excitons in organic semiconductors. *C. R. Physique*, 10:504–13, 2009.
- [23] P. Rinke, A. Schleife, E. Kioupakis, A. Janotti, C. Rödl, F. Bechstedt, M. Scheffler, and C. G. Van de Walle. First-principles optical spectra for f centers in MgO. *Phys. Rev. Lett.*, 108:126404–1–5, 2012.
- [24] S. Huang, Y. Liang, and L. Yang. Exciton spectra in two-dimensional graphene derivatives. *Phys. Rev. B*, 88:075441–1–6, 2013.

- [25] V. Tran, R. Soklaski, Y. Liang, and L. Yang. Layer-controlled band gap and anisotropic excitons in few-layer black phosphorus. *Phys. Rev. B*, 89:235319–1–6, 2014.
- [26] L. Kronik and J. B. Neaton. Excited-state properties of molecular solids from first principles. *Annu. Rev. Phys. Chem.*, 67:587–616, 2016.
- [27] P. Cudazzo, L. Sponza, C. Giorgetti, L. Reining, F. Sottile, and M. Gatti. Exciton band structure in two-dimensional materials. *Phys. Rev. Lett.*, 116:066803–1–6, 2016.
- [28] J. Koskelo, G. Fugallo, M. Hakala, M. Gatti, F. Sottile, and P. Cudazzo. Excitons in van der Waals materials: From monolayer to bulk hexagonal boron nitride. *Phys. Rev. B*, 95:035125–1–14, 2017.
- [29] S. Sharifzadeh. Many-body perturbation theory for understanding optical excitations in organic molecules and solids. *J. Phys.: Condens. Matter*, 20:153002–1–12, 2018.
- [30] X. Gonze, F. Jollet, F. Abreu Araujo, D. Adams, B. Amadon, T. Applencourt, C. Audouze, J.-M. Beuken, J. Bieder, A. Bokhanchuk, E. Bousquet, F. Bruneval, D. Caliste, M. Côté, F. Dahm, F. Da Pieve, M. Delaveau, M. Di Gennaro, B. Dorado, C. Espejo, G. Geneste, L. Genovese, A. Gerossier, M. Giantomassi, Y. Gillet, D.R. Hamann, L. He, G. Jomard, J. Laflamme Janssen, S. Le Roux, A. Levitt, A. Lherbier, F. Liu, I. Lukačević, A. Martin, C. Martins, M.J.T. Oliveira, S. Poncé, Y. Pouillon, T. Rangel, G.-M. Rignanese, A.H. Romero, B. Rousseau, O. Rubel, A.A. Shukri, M. Stankovski, M. Torrent, M.J. Van Setten, B. Van Troeye, M.J. Verstraete, D. Waroquiers, J. Wiktor, B. Xu, A. Zhou, and J.W. Zwanziger. Recent developments in the ABINIT software package. *Comput. Phys. Commun.*, 205:106 – 31, 2016.
- [31] J. Deslippe, G. Samsonidze, D. A. Strubbe, M. Jain, M. L. Cohen, and S. G. Louie. BerkeleyGW: A massively parallel computer package for the calculation of the quasiparticle and optical properties of materials and nanostructures. *Comput. Phys. Commun.*, 183:1269–89, 2012.
- [32] A. Marini, C. Hogan, M. Grüning, and D. Varsano. Yambo: An ab initio tool for excited state calculations. *Comput. Phys. Commun.*, 180:1392–403, 2009.
- [33] D. Sangalli, A. Ferretti, H. Miranda, C. Attaccalite, I. Marri, E. Cannucci, P. Melo, M. Marsili, F. Paleari, A. Marrazzo, G. Prandini, P. Bonfà, M. O. Atambo, F. Affinito, M. Palumbo, A. Molina-Sánchez, C. Hogan, M. Grüning, D. Varsano, and A. Marini. Many-body perturbation theory calculations using the yambo code. *J. Phys.: Condens. Matter*, 31:325902–1–31, 2019.
- [34] C. Vorwerk, B. Aurich, C. Cocchi, and C. Draxl. Bethe–Salpeter equation for absorption and scattering spectroscopy: implementation in the exciting code. *Electron. Struct.*, 1:037001–1–21, 2019.
- [35] E. K. U. Gross and W. Kohn. Local density-functional theory of frequency-dependent linear response. *Phys. Rev. Lett.*, 55:2850–2, 1985. Erratum: *ibid.* **57**, 923 (1986).
- [36] M. Petersilka, U. J. Gossmann, and E. K. U. Gross. Excitation energies from time-dependent density-functional theory. *Phys. Rev. Lett.*, 76:1212–5, 1996.
- [37] M. E. Casida. Time-dependent density functional response theory for molecules. In D. E. Chong, editor, *Recent Advances in Density Functional Methods*, volume 1 of *Recent Advances in Computational Chemistry*, pages 155–92. World Scientific, Singapore, 1995.
- [38] S. Botti, A. Schindlmayr, R. Del Sole, and L. Reining. Time-dependent density functional theory for extended systems. *Rep. Prog. Phys.*, 70:357–407, 2007.
- [39] S. Sharma, J. K. Dewhurst, and E. K. U. Gross. Optical response of extended systems using time-dependent density functional theory. In C. Di Valentin, S. Botti, and M. Cococcioni, editors, *First Principles Approaches to Spectroscopic Properties of Complex Materials*, volume 347 of *Topics in Current Chemistry*, page 235. Springer, Berlin, 2014.
- [40] C. A. Ullrich and Z.-H. Yang. Excitons in time-dependent density-functional theory. In N. Ferré, M. Filatov, and M. Huix-Rotllant, editors, *Density-Functional Methods for Excited States*, volume 368 of *Topics in Current Chemistry*, page 185. Springer, Berlin, 2015.
- [41] V. Turkowski, N. U. Din, and T. S. Rahman. Time-dependent density-functional theory and excitons in bulk and two-dimensional semiconductors. *Computation*, 5:39–1–24, 2017.

- [42] L. Reining, V. Olevano, A. Rubio, and G. Onida. Excitonic effects in solids described by time-dependent density-functional theory. *Phys. Rev. Lett.*, 88:066404–1–4, 2002.
- [43] F. Sottile, V. Olevano, and L. Reining. Parameter-free calculation of response functions in time-dependent density-functional theory. *Phys. Rev. Lett.*, 91:056402–1–4, 2003.
- [44] F. Sottile, K. Karlsson, L. Reining, and F. Aryatesiawan. Macroscopic and microscopic components of exchange-correlation interactions. *Phys. Rev. B*, 68:205112–1–10, 2003.
- [45] A. Marini, R. Del Sole, and A. Rubio. Bound excitons in time-dependent density-functional theory: optical and energy-loss spectra. *Phys. Rev. Lett.*, 91:256402–1–4, 2003.
- [46] R. Del Sole, G. Adragna, V. Olevano, and L. Reining. Long-range behavior and frequency dependence of exchange-correlation kernels in solids. *Phys. Rev. B*, 67:045207–1–5, 2003.
- [47] G. Adragna, R. Del Sole, and A. Marini. Ab initio calculations of the exchange-correlation kernel in extended systems. *Phys. Rev. B*, 68:165108–1–5, 2003.
- [48] R. Stubner, I. V. Tokatly, and O. Pankratov. Excitonic effects in time-dependent density-functional theory: an analytically solvable model. *Phys. Rev. B*, 70:245119–1–12, 2004.
- [49] S. Botti, F. Sottile, N. Vast, V. Olevano, L. Reining, H.-C. Weissker, A. Rubio, G. Onida, R. Del Sole, and R. W. Godby. Long-range contribution to the exchange-correlation kernel of time-dependent density functional theory. *Phys. Rev. B*, 69:155112–1–14, 2004.
- [50] S. Botti, A. Fourreau, F. Nguyen, Y.-O. Renault, F. Sottile, and L. Reining. Energy dependence of the exchange-correlation kernel of time-dependent density-functional theory: a simple model for solids. *Phys. Rev. B*, 72:125203–1–9, 2005.
- [51] F. Sottile, M. Marsili, V. Olevano, and L. Reining. Efficient ab initio calculations of bound and continuum excitons in the absorption spectra of semiconductors and insulators. *Phys. Rev. B*, 76:161103–1–4, 2007.
- [52] G. H. Wannier. The structure of electronic excitation levels in insulating crystals. *Phys. Rev.*, 52:191–7, 1937.
- [53] N. F. Mott. Conduction in polar crystals. II. The conduction band and ultra-violet absorption of alkali-halide crystals. *Trans. Faraday Soc.*, 34:500, 1938.
- [54] G. Dresselhaus. Effective mass approximation for excitons. *J. Phys. Chem. Solids*, 1:14–22, 1956.
- [55] R. J. Elliott. Intensity of optical absorption by excitons. *Phys. Rev.*, 108:1384–9, 1957.
- [56] H. Haug and S. W. Koch. *Quantum Theory of the Optical and Electronic Properties of Semiconductors*. World Scientific, Singapore, 5th edition, 2009.
- [57] Z.-H. Yang, Y. Li, and C. A. Ullrich. A minimal model for excitons within time-dependent density-functional theory. *J. Chem. Phys.*, 137:014513, 2012.
- [58] S. L. Adler. Quantum theory of the dielectric constant in real solids. *Phys. Rev.*, 126:413–20, 1962.
- [59] N. Wiser. Dielectric constant with local field effects included. *Phys. Rev.*, 129:62–9, 1963.
- [60] R. Del Sole and E. Fiorino. Macroscopic dielectric tensor at crystal surfaces. *Phys. Rev. B*, 29:4631–45, 1984.
- [61] T. Sander, E. Maggio, and G. Kresse. Beyond the Tamm-Dancoff approximation for extended systems using exact diagonalization. *Phys. Rev. B*, 92:045209–1–14, 2015.
- [62] Ph. Ghosez, X. Gonze, and R. W. Godby. Long-wavelength behavior of the exchange-correlation kernel in the Kohn-Sham theory of periodic systems. *Phys. Rev. B*, 56:12811–7, 1997.
- [63] Y.-H. Kim and A. Görling. Exact Kohn-Sham exchange kernel for insulators and its long-wavelength behavior. *Phys. Rev. B*, 66:035114–1–6, 2002.
- [64] V. U. Nazarov, G. Vignale, and Y.-C. Chang. Exact dynamical exchange-correlation kernel of a weakly inhomogeneous electron gas. *Phys. Rev. Lett.*, 102:113001–1–4, 2009.
- [65] T. Sander and G. Kresse. Macroscopic dielectric function within time-dependent density functional theory – real time evolution versus the Casida approach. *J. Chem. Phys.*, 146:064110–1–13, 2017.
- [66] I. G. Gurtubay, J. M. Pitarke, W. Ku, A. G. Eguiluz, B. C. Larson, J. Tischler, P. Zschack, and K. D. Finkelstein. Electron-hole and plasmon excitations in 3d transition metals: ab initio

- calculations and inelastic x-ray scattering measurements. *Phys. Rev. B*, 72:125117–1–11, 2005.
- [67] I. V. Tokatly and O. Pankratov. Many-body diagrammatic expansion in a Kohn-Sham basis: implications for time-dependent density functional theory of excited states. *Phys. Rev. Lett.*, 86:2078–81, 2001.
- [68] I. V. Tokatly, R. Stubner, and O. Pankratov. Many-body diagrammatic expansion for the exchange-correlation kernel in time-dependent density functional theory. *Phys. Rev. B*, 65:113107–1–4, 2002.
- [69] S. Kümmel and L. Kronik. Orbital-dependent density functionals: theory and applications. *Rev. Mod. Phys.*, 80:3–60, 2008.
- [70] J. D. Talman and W. F. Shadwick. Optimized effective atomic central potential. *Phys. Rev. A*, 14:36–40, 1976.
- [71] M. Hellgren and U. von Barth. Linear density response function within the time-dependent exact-exchange approximation. *Phys. Rev. B*, 78:115107–1–10, 2008.
- [72] M. Hellgren and U. von Barth. Exact-exchange kernel of time-dependent density functional theory: frequency dependence and photoabsorption spectra of atoms. *J. Chem. Phys.*, 131:044110–1–13, 2009.
- [73] A. Görling. Exact exchange-correlation kernel for dynamic response properties and excitation energies in density-functional theory. *Phys. Rev. A*, 57:3433–6, 1998.
- [74] A. Görling. Exact exchange kernel for time-dependent density-functional theory. *Int. J. Quantum Chem.*, 69:265–77, 1998.
- [75] A. Görling. Exact-exchange methods and perturbation theory. In M. A. L. Marques, C. A. Ullrich, F. Nogueira, A. Rubio, K. Burke, and E. K. U. Gross, editors, *Time-Dependent Density Functional Theory*, volume 706 of *Lecture Notes in Physics*, pages 137–59. Springer, Berlin, 2006.
- [76] F. Bruneval, F. Sottile, V. Olevano, and L. Reining. Beyond time-dependent exact exchange: the need for long-range correlation. *J. Chem. Phys.*, 124:144113–1–9, 2006.
- [77] Y.-H. Kim and A. Görling. Excitonic optical spectrum of semiconductors obtained by time-dependent density-functional theory with the exact-exchange kernel. *Phys. Rev. Lett.*, 89:096402–1–4, 2002.
- [78] S. Cavo, J. A. Berger, and P. Romaniello. Accurate optical spectra of solids from pure time-dependent density-functional theory. *arXiv:1908.00808*, 2019.
- [79] Oleg Gritsenko, Robert van Leeuwen, Erik van Lenthe, and Evert Jan Baerends. Self-consistent approximation to the Kohn-Sham exchange potential. *Phys. Rev. A*, 51:1944–54, 1995.
- [80] M. Kuisma, J. Ojanen, J. Enkovaara, and T. T. Rantala. Kohn-sham potential with discontinuity for band gap materials. *Phys. Rev. B*, 82:115106–1–7, 2010.
- [81] E. J. Baerends. From the Kohn-Sham band gap to the fundamental gap in solids. An integer electron approach. *Phys. Chem. Chem. Phys.*, 19:15639–56, 2017.
- [82] S. Sagmeister and C. Ambrosch-Draxl. Time-dependent density functional theory versus Bethe-Salpeter equation: an all-electron study. *Phys. Chem. Chem. Phys.*, 11:4451–7, 2009.
- [83] Igor Reshetnyak, Matteo Gatti, Francesco Sottile, and Lucia Reining. Excitons on a microscopic level: The mixed dynamic structure factor. *Phys. Rev. Research*, 1:032010–1–6, 2019.
- [84] S. Sharma, J. K. Dewhurst, A. Sanna, and E. K. U. Gross. Bootstrap approximation for the exchange-correlation kernel of time-dependent density-functional theory. *Phys. Rev. Lett.*, 107:186401–1–5, 2011.
- [85] Santiago Rigamonti, Silvana Botti, Valérie Veniard, Claudia Draxl, Lucia Reining, and Francesco Sottile. Estimating excitonic effects in the absorption spectra of solids: Problems and insight from a guided iteration scheme. *Phys. Rev. Lett.*, 114:146402, Apr 2015.
- [86] J. A. Berger. Fully parameter-free calculation of optical spectra for insulators, semiconductors, and metals from a simple polarization functional. *Phys. Rev. Lett.*, 115:137402–1–5, 2015.
- [87] G. Vignale and W. Kohn. Current-dependent exchange-correlation potential for dynamical linear response theory. *Phys. Rev. Lett.*, 77:2037–40, 1996.

- [88] G. Vignale, C. A. Ullrich, and S. Conti. Time-dependent density functional theory beyond the adiabatic local density approximation. *Phys. Rev. Lett.*, 79:4878–81, 1997.
- [89] C. A. Ullrich and G. Vignale. Time-dependent current-density-functional theory for the linear response of weakly disordered systems. *Phys. Rev. B*, 65:245102–1–19, 2002. Erratum: *ibid.* **70**, 239903(E) (2004).
- [90] Z. H. Levine and S. G. Louie. New model dielectric function and exchange-correlation potential for semiconductors and insulators. *Phys. Rev. B*, 25:6310–6, 1982.
- [91] C. Gutle, A. Savin, J. B. Krieger, and J. Chen. Correlation energy contributions from low-lying states to density functionals based on an electron gas with a gap. *Int. J. Quant. Chem.*, 75:885–8, 1999.
- [92] P. E. Trevisanutto, A. Terentjevs, L. A. Constantin, V. Olevano, and F. Della Sala. Optical spectra of solids obtained by time-dependent density functional theory with the jellium-with-gap-model exchange-correlation kernel. *Phys. Rev. B*, 87:205143–1–5, 2013.
- [93] L. A. Constantin and J. M. Pitarke. Simple dynamic exchange-correlation kernel of a uniform electron gas. *Phys. Rev. B*, 75:245127–1–5, 2007.
- [94] C. E. Patrick and K. S. Thygesen. Adiabatic-connection fluctuation-dissipation DFT for the structural properties of solids – The renormalized ALDA and electron gas kernels. *J. Chem. Phys.*, 143:102802, 2015.
- [95] A. V. Terentjev, L. A. Constantin, and J. M. Pitarke. Gradient-dependent exchange-correlation kernel for materials optical properties. *Phys. Rev. B*, 98:085123–1–12, 2018.
- [96] D. Jacquemin, V. Wathelet, E. A. Perpète, and C. Adamo. Extensive TD-DFT benchmark: singlet-excited states of organic molecules. *J. Chem. Theor. Comput.*, 5:2420–35, 2009.
- [97] D. Jacquemin, E. A. Perpète, I. Ciofini, and C. Adamo. Assessment of functionals for TD-DFT calculations of singlet-triplet transitions. *J. Chem. Theor. Comput.*, 6:1532–7, 2010.
- [98] Y.-M. Byun and C. A. Ullrich. Excitons in solids from time-dependent density-functional theory: Assessing the Tamm-Dancoff approximation. *Computation*, 5:9, 2017.
- [99] Y.-M. Byun and C. A. Ullrich. Assessment of long-range-corrected exchange-correlation kernels for solids: Accurate exciton binding energies via an empirically scaled bootstrap kernel. *Phys. Rev. B*, 95:205136–1–11, 2017.
- [100] Kurt Lejaeghere, Gustav Bihlmayer, Torbjörn Björkman, Peter Blaha, Stefan Blügel, Volker Blum, Damien Caliste, Ivano E. Castelli, Stewart J. Clark, Andrea Dal Corso, Stefano de Gironcoli, Thierry Deutsch, John Kay Dewhurst, Igor Di Marco, Claudia Draxl, Marcin Dulak, Olle Eriksson, José A. Flores-Livas, Kevin F. Garrity, Luigi Genovese, Paolo Giannozzi, Matteo Giantomassi, Stefan Goedecker, Xavier Gonze, Oscar Grånäs, E. K. U. Gross, Andris Gulans, François Gygi, D. R. Hamann, Phil J. Hasnip, N. A. W. Holzwarth, Diana Iuşan, Dominik B. Jochym, François Jollet, Daniel Jones, Georg Kresse, Klaus Koepernik, Emine Küçükbenli, Yaroslav O. Kvashnin, Inka L. M. Loch, Sven Lubeck, Martijn Marsman, Nicola Marzari, Ulrike Nitzsche, Lars Nordström, Taisuke Ozaki, Lorenzo Paulatto, Chris J. Pickard, Ward Poelmans, Matt I. J. Probert, Keith Refson, Manuel Richter, Gian-Marco Rignanese, Santanu Saha, Matthias Scheffler, Martin Schlipf, Karlheinz Schwarz, Sangeeta Sharma, Francesca Tavazza, Patrik Thunström, Alexandre Tkatchenko, Marc Torrent, David Vanderbilt, Michiel J. van Setten, Veronique Van Speybroeck, John M. Wills, Jonathan R. Yates, Guo-Xu Zhang, and Stefaan Cottenier. Reproducibility in density functional theory calculations of solids. *Science*, 351(6280):aad3000–1–7, 2016.
- [101] P. Giannozzi, O. Andreussi, T. Brumme, O. Bunau, M. Buongiorno Nardelli, M. Calandra, R. Car, C. Cavazzoni, D. Ceresoli, M. Cococcioni, N. Colonna, I. Carnimeo, A. Dal Corso, S. de Gironcoli, P. Delugas, R. A. DiStasio Jr, A. Ferretti, A. Floris, G. Fratesi, G. Fugallo, R. Gebauer, U. Gerstmann, F. Giustino, T. Gorni, J. Jia, M. Kawamura, H.-Y. Ko, A. Kokalj, E. Küçükbenli, M. Lazzeri, M. Marsili, N. Marzari, F. Mauri, N. L. Nguyen, H.-V. Nguyen, A. Otero de-la Roza, L. Paulatto, S. Poncé, D. Rocca, R. Sabatini, B. Santra, M. Schlipf, A. P. Seitsonen, A. Smogunov, I. Timrov, T. Thonhauser, P. Umari, N. Vast, X. Wu, and S. Baroni. Advanced capabilities for

- materials modelling with QUANTUM ESPRESSO. *J. Phys.: Condens. Matter*, 29(46):465901, 2017.
- [102] Z. H. Levine and D. C. Allan. Linear optical response in silicon and germanium including self-energy effects. *Phys. Rev. Lett.*, 63:1719–22, 1989.
- [103] X. Gonze and C. Lee. Dynamical matrices, Born effective charges, dielectric permittivity tensors, and interatomic force constants from density-functional perturbation theory. *Phys. Rev. B*, 55:10355–68, 1997.
- [104] J. Heyd, J. E. Peralta, G. E. Scuseria, and R. L. Martin. Energy band gaps and lattice parameters evaluated with the Heyd-Scuseria-Ernzerhof screened hybrid functional. *J. Chem. Phys.*, 112:174101–1–8, 2005.
- [105] I. C. Gerber, J. G. Ángyán, M. Marsman, and G. Kresse. Range separated hybrid density functional with long-range Hartree-Fock exchange applied to solids. *J. Chem. Phys.*, 127:054101–1–9, 2007.
- [106] T. M. Henderson, J. Paier, and G. E. Scuseria. Accurate treatment of solids with the HSE screened hybrid. *Phys. Stat. Solidi B*, 248:767–74, 2011.
- [107] M. Jain, J. R. Chelikowsky, and S. G. Louie. Reliability of hybrid functionals in predicting band gaps. *Phys. Rev. Lett.*, 107:216806–1–5, 2011.
- [108] M. A. L. Marques, J. Vidal, M. J. T. Oliveira, L. Reining, and S. Botti. Density-based mixing parameter for hybrid functionals. *Phys. Rev. B*, 83:035119–1–5, 2011.
- [109] Y.-I. Matsushita, K. Nakamura, and A. Oshiyama. Comparative study of hybrid functionals applied to structural and electronic properties of semiconductors and insulators. *Phys. Rev. B*, 84:075205–1–13, 2011.
- [110] J. E. Moussa, P. A. Schultz, and J. R. Chelikowsky. Analysis of the Heyd-Scuseria-Ernzerhof density functional parameter space. *J. Chem. Phys.*, 136:204117–1–10, 2012.
- [111] C. Friedrich, M. Betzinger, M. Schlipf, S. Blügel, and A. Schindlmayr. Hybrid functionals and GW approximation in the FLAPW method. *J. Phys.: Condens. Matter*, 24:293201–1–24, 2012.
- [112] J. H. Skone, M. Govoni, and G. Galli. Self-consistent hybrid functional for condensed systems. *Phys. Rev. B*, 89:195112–1–12, 2014.
- [113] J. H. Skone, M. Govoni, and G. Galli. Nonempirical range-separated hybrid functionals for solids and molecules. *Phys. Rev. B*, 93:235106–1–12, 2016.
- [114] M. Gerosa, C. E. Bottani, L. Caramella, G. Onida, C. Di Valentin, and G. Pacchioni. Electronic structure and phase stability of oxide semiconductors: Performance of dielectric-dependent hybrid functional DFT, benchmarked against GW band structure calculations and experiments. *Phys. Rev. B*, 91:155201–1–15, 2015.
- [115] Y. Hinuma, Y. Kumagai, I. Tanaka, and F. Oba. Band alignment of semiconductors and insulators using dielectric-dependent hybrid functionals: Toward high-throughput evaluation. *Phys. Rev. B*, 95:075302–1–10, 2017.
- [116] W. Chen, G. Miceli, G.-M. Rignanese, and A. Pasquarello. Nonempirical dielectric-dependent hybrid functional with range separation for semiconductors and insulators. *Phys. Rev. Materials*, 2:073803–1–14, 2018.
- [117] R. Del Sole and R. Girlanda. Optical properties of semiconductors within the independent-quasiparticle approximation. *Phys. Rev. B*, 48:11789–95, 1993.
- [118] M. Shao, F. H. da Jornada, C. Yang, J. Deslippe, and S. G. Louie. Structure preserving parallel algorithms for solving the Bethe-Salpeter eigenvalue problem. *Linear Algebra Its Appl.*, 488:148–67, 2017.
- [119] S. Sharma, J. K. Dewhurst, A. Sanna, and E. K. U. Gross. Comment on “Estimating excitonic effects in the absorption spectra of solids: Problems and insight from a guided iteration scheme”. *Phys. Rev. Lett.*, 117:159701, 2016.
- [120] Santiago Rigamonti, Silvana Botti, Valérie Veniard, Claudia Draxl, Lucia Reining, and Francesco Sottile. Rigamonti *et al.* reply:. *Phys. Rev. Lett.*, 117:159702, Oct 2016.
- [121] Z.-H. Yang and C. A. Ullrich. Direct calculation of exciton binding energies with time-dependent

- density-functional theory. *Phys. Rev. B*, 87:195204, 2013.
- [122] G. Swetha, V. Kanchana, and M. C. Valsakumar. Excitonic effects in oxyhalide scintillating host compounds. *J. Appl. Phys.*, 116:133510–1–9, 2014.
- [123] S. Sharma, J. K. Dewhurst, S. Shallcross, G. K. Madjarova, and E. K. U. Gross. Excitons in organics using time-dependent density functional theory: PPV, pentacene, and picene. *J. Chem. Theor. Comput.*, 11:1710–4, 2015.
- [124] M. Dadsetani and A. R. Omid. Ab initio study on optical properties of glycine sodium nitrate: a novel semiorganic nonlinear optical crystal. *RSC Adv.*, 5:90559–69, 2015.
- [125] M. Friedrich, W. G. Schmidt, A. Schindlmayr, and S. Sanna. Optical properties of titanium-doped lithium niobate from time-dependent density-functional theory. *Phys. Rev. Materials*, 1:034401–1–7, 2017.
- [126] M. Friedrich, W. G. Schmidt, A. Schindlmayr, and S. Sanna. Polaron optical absorption in congruent lithium niobate from time-dependent density-functional theory. *Phys. Rev. Materials*, 1:054406–1–5, 2017.
- [127] W. F. Espinosa-García, J. M. Osorio-Guillén, and C. M. Araujo. Dimension-dependent band alignment and excitonic effects in graphitic carbon nitride: a many-body perturbation and time-dependent density functional theory study. *RSC Adv.*, 7:44997–5002, 2017.
- [128] W. F. Espinosa-García, S. Pérez-Walton, J. M. Osorio-Guillén, and C. M. Araujo. The electronic and optical properties of the sulvanite compounds: a many-body perturbation and time-dependent density functional theory study. *J. Phys.: Condens. Matt.*, 30:035502–1–8, 2018.
- [129] N. Gauriot, V. Vénier, and E. Luppi. Long-range corrected exchange-correlation kernels to describe excitons in second-harmonic generation. *J. Chem. Phys.*, 151:234111–1–12, 2019.
- [130] J. Paier, M. Marsman, and G. Kresse. Dielectric properties and excitons for extended systems from hybrid functionals. *Phys. Rev. B*, 78:121201(R)–1–4, 2008.
- [131] L. Bernasconi, S. Tomić, M. Ferrero, M. Rérat, R. Orlando, R. Dovesi, and N. M. Harrison. First-principles optical response of semiconductors and oxide materials. *Phys. Rev. B*, 83:195325, 2011.
- [132] S. Tomić, L. Bernasconi, B. G. Searle, and N. M. Harrison. Electronic and optical structure of wurtzite CuInS_2 . *J. Phys. Chem. C*, 118:14478, 2014.
- [133] R. Webster, L. Bernasconi, and N. M. Harrison. Optical properties of alkali halide crystals from all-electron hybrid TD-DFT calculations. *J. Chem. Phys.*, 142:214705–1–11, 2015.
- [134] S. Refaely-Abramson, M. Jain, S. Sharifzadeh, J. B. Neaton, and L. Kronik. Solid-state optical absorption from optimally tuned time-dependent range-separated hybrid density functional theory. *Phys. Rev. B*, 92:081204(R)–1–6, 2015.
- [135] D. Wing, J. B. Haber, R. Noff, B. Barker, D. A. Egger, A. Ramasubramaniam, S. G. Louie, J. B. Neaton, and L. Kronik. Comparing time-dependent density functional theory with many-body perturbation theory for semiconductors: Screened range-separated hybrids and the GW plus Bethe-Salpeter approach. *Phys. Rev. Materials*, 3:064603–1–10, 2019.
- [136] A. Ramasubramaniam, D. Wing, and L. Kronik. Transferable screened range-separated hybrids for layered materials: The cases of MoS_2 and h-BN. *Phys. Rev. Materials*, 3:084007–1–8, 2019.
- [137] Z.-H. Yang, F. Sottile, and C. A. Ullrich. A simple screened exact-exchange approach for excitonic properties in solids. *Phys. Rev. B*, 92:035202, 2015.
- [138] J. Sun, J. Yang, and C. A. Ullrich. Low-cost alternatives to the Bethe-Salpeter equation: towards simple hybrid functionals for excitonic effects in solids. *Phys. Rev. Research*, 2:013091–1–13, 2020.
- [139] G. Cappellini, R. Del Sole, Lucia Reining, and F. Bechstedt. Model dielectric function for semiconductors. *Phys. Rev. B*, 47:9892–5, 1993.
- [140] G. F. Bertsch, J.-I. Iwata, A. Rubio, and K. Yabana. Real-space, real-time method for the dielectric function. *Phys. Rev. B*, 62:7998–8002, 2000.
- [141] K. Yabana, T. Nakatsukasa, J.-I. Iwata, and G. F. Bertsch. Real-time, real-space implementation of the linear response time-dependent density-functional theory. *phys. stat. sol. (b)*, 243:1121–

- 38, 2006.
- [142] K. Yabana, T. Sugiyama, Y. Shinohara, T. Otobe, and G. F. Bertsch. Time-dependent density functional theory for strong electromagnetic fields in crystalline solids. *Phys. Rev. B*, 85:045134–1–11, 2012.
- [143] A. Yamada and K. Yabana. Multiscale time-dependent density functional theory for a unified description of ultrafast dynamics: Pulsed light, electron, and lattice motions in crystalline solids. *Phys. Rev. B*, 99:245103–1–10, 2019.
- [144] C. D. Pemmaraju, F. D. Vila, J. J. Kas, S. A. Sato, J. J. Rehr, K. Yabana, and D. Prendergast. Velocity-gauge real-time TDDFT within a numerical atomic orbital basis set. *Comput. Phys. Commun.*, 226:30–8, 2018.
- [145] C. D. Pemmaraju. Valence and core excitons in solids from velocity-gauge real-time TDDFT with range-separated hybrid functionals: An LCAO approach. *Comput. Condens. Matter*, 16:e00348–1–13, 2018.
- [146] N. Tancogne-Dejean, O. D. Mücke, F. X. Kärtner, and A. Rubio. Impact of the electronic band structure in high-harmonic generation spectra of solids. *Phys. Rev. Lett.*, 118:087403–1–6, 2017.
- [147] N. Tancogne-Dejean, O. D. Mücke, F. X. Kärtner, and A. Rubio. Ellipticity dependence of high-harmonic generation in solids originating from coupled intraband and interband dynamics. *Nature Commun.*, 8:745–1–10, 2017.